

# Near-IR Galaxy Counts and Evolution from the Wide-Field ALHAMBRA survey<sup>1</sup>

D. Cristóbal-Hornillos<sup>1</sup>, J. A. L. Aguerri<sup>2</sup>, M. Moles<sup>1</sup>, J. Perea<sup>1</sup>, F. J. Castander<sup>5</sup>, T. Broadhurst<sup>3</sup>, E. J. Alfaro<sup>1</sup>, N. Benítez<sup>1,11</sup>, J. Cabrera-Caño<sup>4</sup>, J. Cepa<sup>2,6</sup>, M. Cerviño<sup>1</sup>, A. Fernández-Soto<sup>12</sup>, R. M. González Delgado<sup>1</sup>, C. Husillos<sup>1</sup>, L. Infante<sup>8</sup>, I. Márquez<sup>1</sup>, V. J. Martínez<sup>7,9</sup>, J. Masegosa<sup>1</sup>, A. del Olmo<sup>1</sup>, F. Prada<sup>1</sup>, J. M. Quintana<sup>1</sup>, and S. F. Sánchez<sup>10</sup>

dch@iaa.es, jalfonso@iac.es, moles@iaa.es,  
jaime@iaa.es, fjc@ieec.fcr.es, emilio@iaa.es, benitez@iaa.es,  
tjb@wise1.tau.ac.il, jcc-famn@us.es, jcn@iac.es, mcs@iaa.es,  
alberto.fernandez@uv.es, rosa@iaa.es, cesar@iaa.es, linfante@astro.puc.cl,  
isabel@iaa.es, vicent.martinez@uv.es, pepa@iaa.es, chony@iaa.es,  
fprada@iaa.es, quintana@iaa.es, sanchez@caha.es

## ABSTRACT

The ALHAMBRA survey aims to cover 4 square degrees using a system of 20 contiguous, equal width, medium-band filters spanning the range 3500 Å to 9700 Å plus the standard JHKs filters. Here we analyze deep near-IR number counts of one of our fields (ALH08) for which we have a relatively large area (0.5 square degrees) and faint photometry (J=22.4, H=21.3 and K=20.0 at the

---

<sup>1</sup>Instituto de Astrofísica de Andalucía, CSIC, Apdo. 3044, E-18080 Granada

<sup>2</sup>Instituto de Astrofísica de Canarias, La Laguna, Spain

<sup>3</sup>School of Physics and Astronomy, Tel Aviv University, Israel

<sup>4</sup>Departamento de Física Atómica, Molecular y Nuclear, Facultad de Física, Universidad de Sevilla, Spain

<sup>5</sup>Institut de Ciències de l'Espai, IEEC-CSIC, Barcelona, Spain

<sup>6</sup>Departamento de Astrofísica, Facultad de Física, Universidad de la Laguna, Spain

<sup>7</sup>Departament d'Astronomia i Astrofísica, Universitat de València, València, Spain

<sup>8</sup>Departamento de Astronomía, Pontificia Universidad Católica, Santiago, Chile

<sup>9</sup>Observatori Astronòmic de la Universitat de València, València, Spain

<sup>10</sup>Centro Astronómico Hispano-Alemán, Almería, Spain

<sup>11</sup>IFF(CSIC), C/Serrano 113-bis, 28005 Madrid, Spain

<sup>12</sup>Instituto de Física de Cantabria (CSIC), 39005 Santander, Spain

50% of recovery efficiency for point-like sources). We find that the logarithmic gradient of the galaxy counts undergoes a distinct change to a flatter slope in each band: from 0.44 at [17.0, 18.5] to 0.34 at [19.5, 22.0] for the J band; for the H band 0.46 at [15.5, 18.0] to 0.36 at [19.0, 21.0], and in Ks the change is from 0.53 in the range [15.0, 17.0] to 0.33 in the interval [18.0, 20.0]. These observations together with faint optical counts are used to constrain models that include density and luminosity evolution of the local type-dependent luminosity functions. Our models imply a decline in the space density of evolved early-type galaxies with increasing redshift, such that only 30% - 50% of the bulk of the present day red-ellipticals was already in place at  $z \sim 1$ .

*Subject headings:* cosmology: observations — galaxies: photometry — galaxies: evolution — surveys — galaxies: high-redshift — infrared: galaxies

## 1. Introduction

It is well understood that the stellar masses of galaxies are better examined with near-IR (NIR) observations compared to shorter wavelengths mainly because the near-IR light is relatively less affected by recent episodes of star formation and by internal dust extinction. Moreover, the K-corrections are also smaller and better constrained in the NIR and hence massive high redshift objects are relatively prominent in the NIR. Despite this relative insensitivity to luminosity evolution and the effects of dust, the hope of using the NIR counts to constrain the cosmological parameters (Gardner et al. 1993; Moustakas et al. 1997; Huang et al. 2001; Metcalfe et al. 2001) has not proved feasible because evolution in the space density of galaxies was soon understood to be of comparable significance for the NIR counts as the cosmological curvature (Broadhurst et al. 1992).

Disentangling the effects of cosmology from evolution is not straightforward even in the NIR, and now it has become more appropriate to turn the question around and make use of the impressive constraints on the cosmological parameters from WMAP (Spergel et al. 2003), and type Ia supernovae (Riess et al. 1998; Perlmutter et al. 1999), in order to measure more carefully the rate of evolution (Martini 2001; Saracco et al. 2001; Cristóbal-Hornillos et al. 2003; Eliche-Moral et al. 2006). In addition, imaging in the NIR has progressed well with

---

<sup>1</sup>Based on observations collected at the German-Spanish Astronomical Center, Calar Alto, jointly operated by the Max-Planck-Institut für Astronomie Heidelberg and the Instituto de Astrofísica de Andalucía (CSIC).

fully cryogenic wide-field imagers now available on several 4m class telescopes. We also have at our disposal now much better estimates of the luminosity functions of different classes of galaxies from the large local redshift surveys in particular the SDSS (Blanton et al. 2003; Nakamura et al. 2003), or 2dFGRS (Cole et al. 2001).

The evolution of the luminosity functions has been addressed making use of spectroscopic redshift surveys. However, the results of those studies differ due to the limitations in terms of low statistic, or small fields probed which lead to uncertainties due to the large scale structure. In Fontana et al. (2004) a mild (20-30%) evolution in the number density of massive objects since  $z \sim 1$  is found. Also a roughly constant number density for red galaxies to  $z = 0.8$  is found in Im et al. (2002). Using COMBO-17 photometric redshift information (Wolf et al. 2003), and the rest-frame color bimodality at each redshift, Bell et al. (2004) with a sample of  $\sim 25000$  galaxies, concluded that the stellar mass in red-galaxies has increase in a factor 2-3 from  $z \sim 1$  to the present. Combining spectroscopic with photometric redshift data Ilbert et al. (2006) point to an increase in a factor of  $\sim 2.7$  for the density of red bulge-dominated galaxies between  $z = 1$  and  $z = 0.6$ . Faber et al. (2007) found a different evolution since  $z \sim 1$  in number densities in the red and blue galaxy population, being constant for the blue galaxies, while the number density of the red galaxies increases in a factor 3. Wide field imaging with larger covered area, and greater numbers selected to uniform faint limits is complementary to the redshift surveys in examining statistical models proposed for evolution.

In practical terms it is most useful to combine faint NIR counts with deep blue counts when examining models of evolution to contrast the effects of luminosity and density evolution which affect these two spectral ranges in different ways. In McCracken et al. (2000); Metcalfe et al. (2001) the authors use non-evolving models with a higher  $\phi^*$  normalization in the B-band even if this leads to an over-prediction of bright galaxies than is observed. Huang et al. (2001) pointed out that both the optical and NIR counts present an excess over the no-evolution models, finding passive evolution models more suitable to match the distributions. The authors emphasize nevertheless their disappointment with the fact that in the passive evolution models the faint number counts are dominated by early-type galaxies, whereas the real data show that spiral and Sd/Irr galaxies are the main contributors to the faint counts even in the K-band.

A characteristic feature of the NIR galaxy counts reported in several works (Gardner et al. 1993; Huang et al. 2001; Cristóbal-Hornillos et al. 2003; Iovino et al. 2005) is the change of slope at  $17 \leq Ks \leq 18$ . This distinctive flattening is not observed in the B-band counts. This effect has been interpreted in terms of a change in the dominant galaxy population, becoming increasingly dominated by an intrinsically bluer population (Gardner et al. 1993;

Eliche-Moral et al. 2006). In the model described in Cristóbal-Hornillos et al. (2003) a delay in the formation of the bulk of the early-type galaxies to  $z_{form} < 2$  and the presence of a dwarf star-forming population are invoked to match the Ks-band counts. A similar dwarf star-forming population at  $z > 1$ , that is not present at lower redshift was found compatible in Metcalfe et al. (1996, 2001) but that work uses a  $q_0 = 0.5, \Lambda = 0.0$  cosmology, requiring some revision.

Alternatively, an increase of  $\phi^*$  for late-type galaxies, driven via mergers, can produce similar results without introducing an ad hoc population that is unseen in the local LFs (Eliche-Moral et al. 2006). In any case, a low  $z_{form} \sim 1.5$  for the ellipticals remains necessary to generate a significant decrease in the number of red galaxies and to account for the distinctive break in the NIR count slope at Ks $\sim$ 17.5.

Here we use the NIR data from the first completed ALHAMBRA field, hereafter ALH08 (details of the project can be found in Moles et al. (2008) and <http://www.iaa.es/alhambra>). The limiting magnitudes (at S/N=5 in an aperture diameter of  $2 \times \text{FWHM}$ ) reached in the 3 NIR bands are in mean for the eight frames in ALH8: J=22.6, H=21.5 and Ks=20.1 with a 0.3 rms (Vega system), and the total area covered amounts to  $\sim 0.5$  square degrees. The completed survey will cover 8 independent fields with a total area of 4 square degrees. The ALHAMBRA survey occupies a middle ground in terms of the product of depth and area in all three standard NIR filters. The bright end of the counts is well constrained by our relatively large area allowing a careful examination of the location and size of the break in the count-slopes in J,H and Ks at fainter magnitudes. We have paid special attention to S/G separation, which at the intermediate magnitude range, is effectively achieved using optical-NIR color indices by combining our ALH08 NIR data with the corresponding Sloan DR5 data.

Unless specified otherwise, all magnitudes here are presented in the Vega system, and the favored cosmological model, with  $H_0 = 70 \text{ km s}^{-1} \text{ Mpc}^{-1}$ ,  $\Omega_M = 0.3$ ,  $\Omega_\Lambda = 0.7$  was adopted through this paper.

## 2. Observing Strategy and Data Reduction

The ALHAMBRA survey is collecting data in 23 optical-NIR filters using the Calar Alto 3.5m telescope with the cameras LAICA for the 20 optical filters, and OMEGA2000 for the NIR, JHKs filters (Moles et al. 2008; Benitez et al. 2008). In this paper we discuss the galaxy number counts in the J, H and Ks bands computed in the completed ALH08 pointing. Due to the OMEGA2000 and LAICA geometries, two parallel strips of  $\sim 1$  degree

$\times 0.25$  degrees are acquired in each of the eight ALHAMBRA fields. Each of these strips is covered by four OMEGA2000 pointings. Fig. 1 shows the central part of the processed image for one such pointing in ALH08.

The OMEGA2000 camera has a focal plane array of type HAWAII-2 by Rockwell with  $2048 \times 2048$  pixels. The plate scale is  $0.45$  arcsec/pixel, giving a full field of view of  $\sim 236$  arcmin<sup>2</sup>. The JHKs images were taken using a dither pattern of 20 positions, with single images time exposures of 80 s in J, 60 s in H and 46 s in Ks band (obtained using respectively 16, 20 and 23 software co-adds). The total exposure time was 5 ks in each of the three filters.

Due to the high quantity of raw data images we have implemented a dedicated reduction pipeline to process the images. This code will be presented and discussed in a forthcoming technical paper. The use of the reduction pipeline guaranties the homogeneity of the process, and allows us to perform a first automatic analysis of the resulting images and to verify the quality of the products in real time. The magnitude at the 50% of recovery efficiency for point-like sources in the eight final images corresponds in average to  $J = 22.4 \pm 0.24$ ,  $H = 21.3 \pm 0.14$  and  $Ks = 20.0 \pm 0.13$  in the Vega system. The galaxy number counts have been computed in the high signal to noise region of the final images, covering a total of  $\sim 1600$  arcmin<sup>2</sup>, or  $0.45$  sq deg.

## 2.1. Flat-fielding and sky subtraction

Firstly, the individual images of each observing run were dark-subtracted, and flat-fielded by super-flat images constructed with the science images in each filter. In the case of NIR imaging it is specially important to remove properly the high sky level that is changing in short timescales. The sky structure of each image was removed with the XDIMSUM package (Stanford et al. 1995) with a sky image constructed with the median of the 6 images closest in acquisition time, which in the case of the J, H, Ks filters correspond to timescales of 480, 360, 276 s respectively. During this process cosmic ray masks for each individual image were also created.

SExtractor (Bertin & Arnouts 1996) was used with the preliminary sky subtracted images to compute the number of detected objects (above a given S/N and with ellipticity lower than a certain limit), and to make a robust estimate of the FWHM of each image. This information together with the sky level variation was used to automatically remove low S/N images, lying outside the survey requirements, and also to identify exposures presenting problems such as telescope trailing.

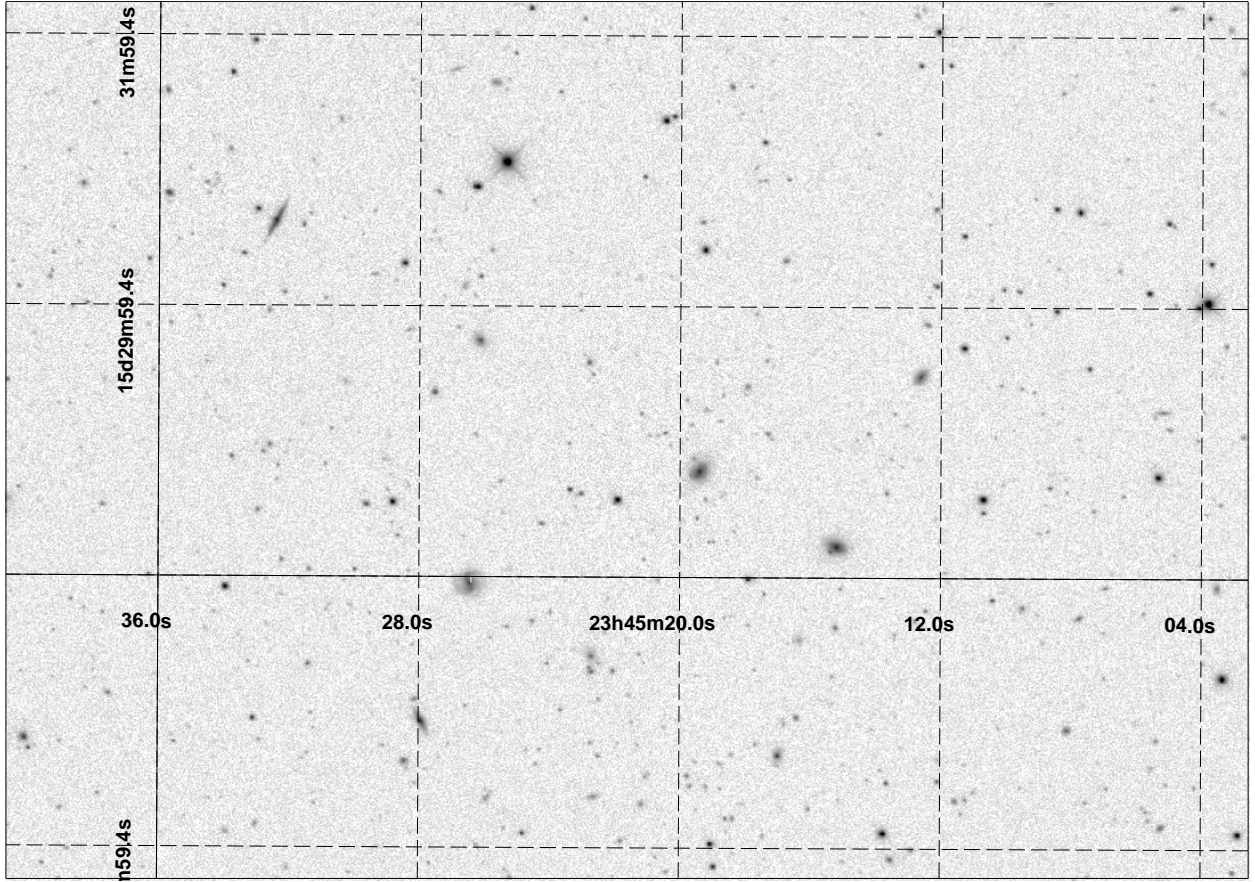


Fig. 1.— Central part ( $\sim 9.2' \times 6.4'$ ) of one of the pointings in the ALH08 field in the Ks band.

## 2.2. Ghost and linear pattern masks

The readout of the detector array produces ghost images coming from bright stars. As those spurious effects are replicated in all the readout channels (separated by 128 pixels) of the detector’s quadrant where the real bright source is located, it was possible to mask them before image combination.

Linear patterns produced by moving objects were located in the images using two different approaches: i) Objects with high ellipticity and pixel area were identified from the individual image SExtractor catalogs. ii) Linear patterns split in multiple spots and structures were located using the Hough transform. Linear patterns detected by any of the two methods were masked.

## 2.3. Image combination

Using XDIMSUM, the images were combined masking the cosmic rays, bad pixels and linear patterns. Those preliminary co-added images were used to create object and bright cores masks. Object masks were used to cover the sources in the second iteration of the XDIMSUM sky subtraction procedure. Bright cores masks operate when constructing an improved version of the cosmic ray masks.

At this point, the individual images have been dark current corrected, flat fielded and sky subtracted. Each individual image has an associated mask containing the bad pixels, cosmic rays, linear patterns and ghost images.

To perform the final combination of the processed images we used SWARP (Bertin et al. 2002), a code that combines the images, correcting at the same time the geometrical distortions in the individual images using the information stored in WCS headers. The astrometric calibration of each individual image and the update of its WCS headers was done by the pipeline using an automatic module. During the SWARP combination the extinction variations among the images were also corrected. More technical details on the image combination are given in appendix A.

## 2.4. Photometric calibration

For the photometric calibration we used the 2MASS catalogs (Cutri et al. 2003). After having combined all the images of each pointing, the objects in common with the 2MASS catalogs were found and those with higher signal to noise ratio selected to compute a zero

point offset.

In Fig. 2 an example of the photometric calibration for one of the pointings in ALH08 is shown. The histogram with the rms in the photometric calibration for the ALH08 pointings in the three NIR bands is shown in Fig. 3. The mean value for the rms is  $0.028 \pm 0.006$  mags, and a mean of 36 calibration sources have been used in each frame. We have not found any appreciable color related trend.

The calibrated images were inspected for the possible presence of ring patterns that would have been produced by pupil ghosts. We computed for each band, and for all the sources used in the calibration process of the different final frames, the difference between our photometry and the 2MASS photometry as a function of the radial distance to the nominal field center.

We found a significant effect, over 0.02 mags only in the J-band images, as it is shown in Fig. 4. This effect was corrected by fitting the pupil ghost, using the `mscpupil` task in the IRAF MSCRED package (Valdes 2002), and removing this pupil image from the flat-fields and individual images. The final resulting radial differences are shown for the J band in Fig. 5 where it clearly appears that all the systematics was corrected well below the  $1\sigma$  level.

### 3. Galaxy Number Counts

The steps to compute robust counts to the 50% detection level of the images are similar to those described in Cristóbal-Hornillos et al. (2003) and in Eliche-Moral et al. (2006). In the next section we detail how the best set of SExtractor parameters was estimated as a compromise between optimizing the depth at the 50% completeness level while keeping low the number of spurious sources.

#### 3.1. Completeness corrections

In order to compute the corrections that should be applied to the faint part of the galaxy counts we have performed a set of Monte Carlo simulations where real sources from the images were injected back to the same science image at different positions. The completeness correction to be applied depends on the surface brightness profile of the source. To account for this we computed a different correction function for sources in three effective radius ( $Re$ ) intervals. Those  $Re$  intervals in pixels for the simulations were chosen from the histogram of the Fig. 6 (top panel):  $Re \leq 1.75$ ,  $1.75 < Re \leq 2.25$  and  $Re > 2.25$ . In Fig. 6 (bottom panel) it is shown how the  $Re$  recovered decreases as the magnitude goes fainter (see below



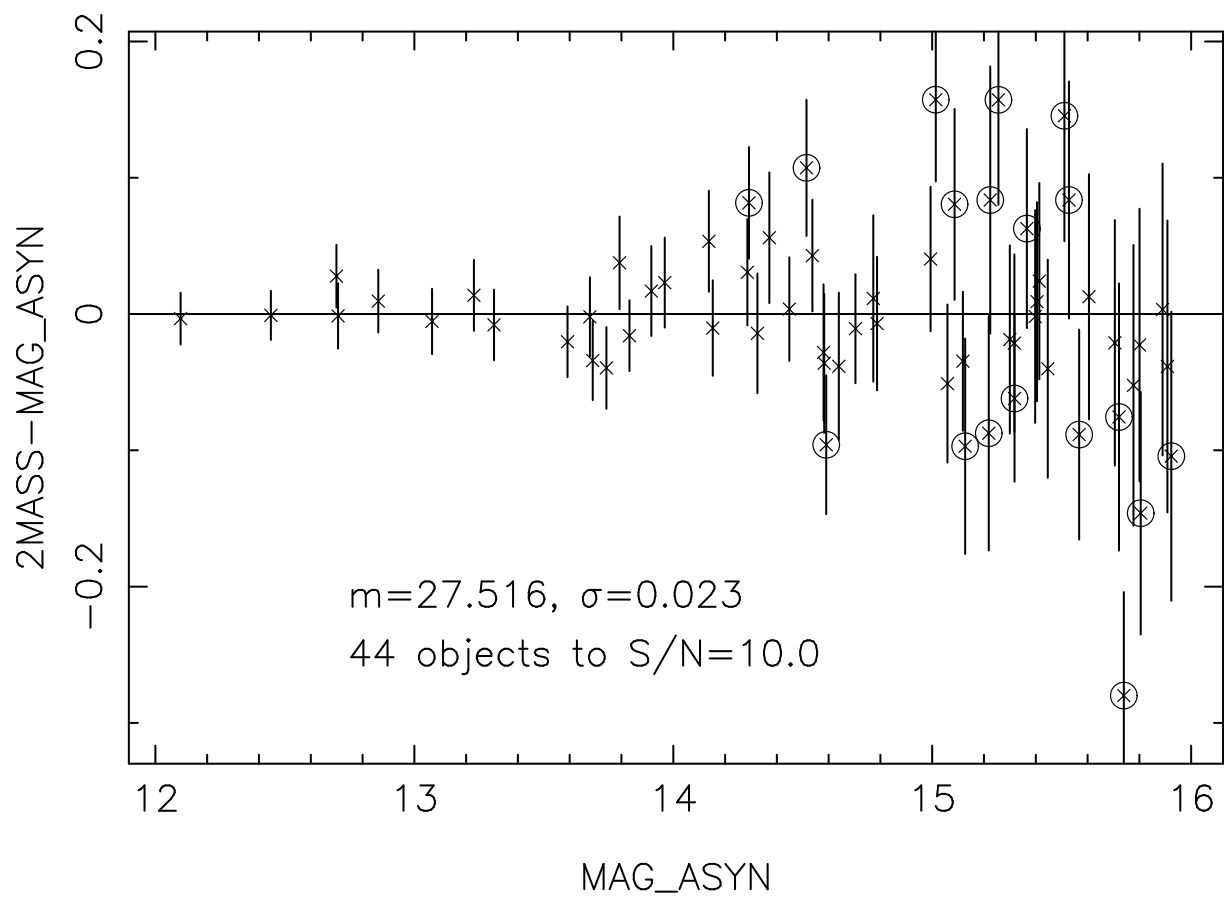


Fig. 2.— Calibration with 2MASS stars for the one of the pointings included in the ALH08 field in the H filter. Sources marked with a circle were eliminated using a  $2\sigma$  reject in the calibration fit. Error bars correspond to the 2MASS magnitude error summed in quadrature with the SExtractor computed error.

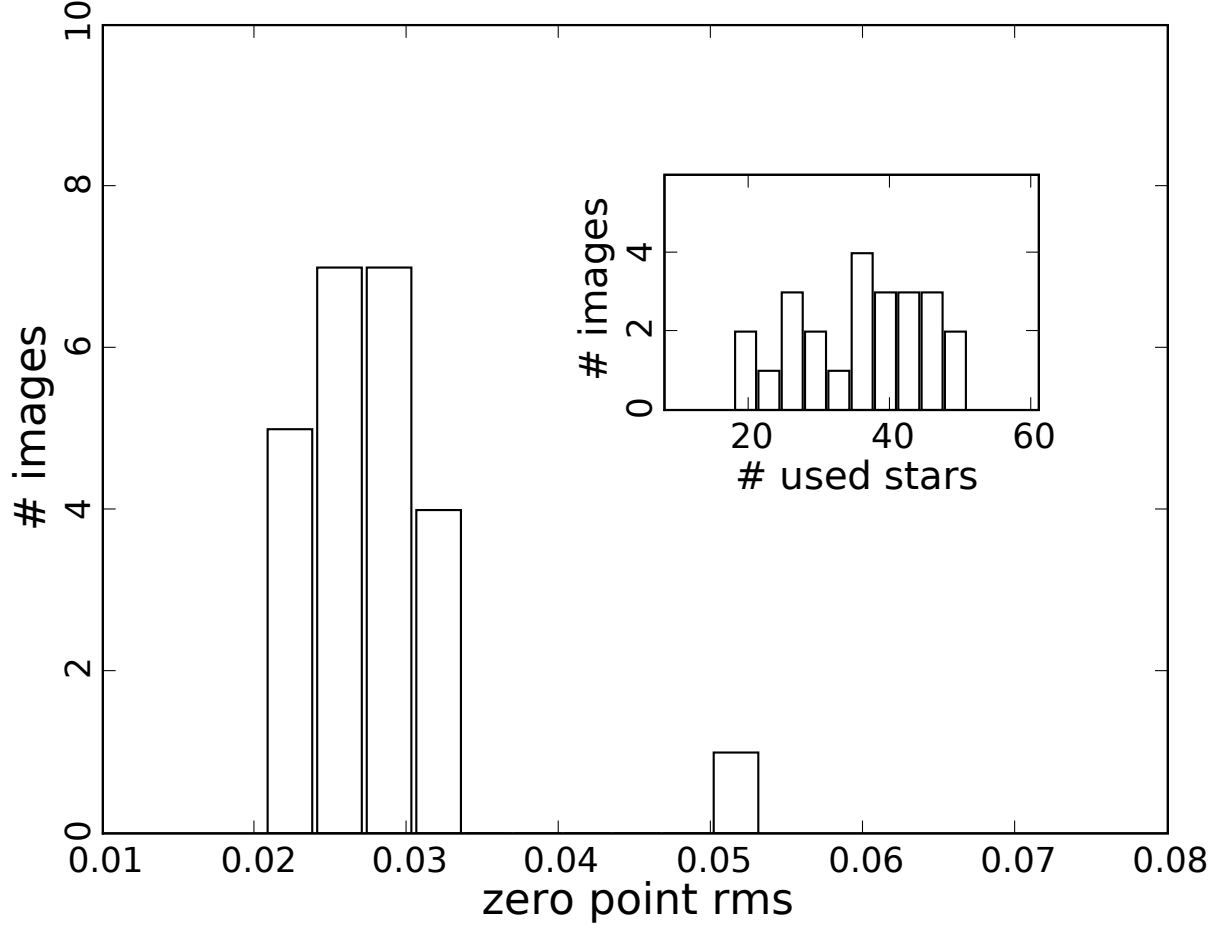


Fig. 3.— Histogram of the photometric accuracy of the different pointings in the ALH08 field. In the small panel the histogram of the number of used stars for the calibration in each pointing is shown.

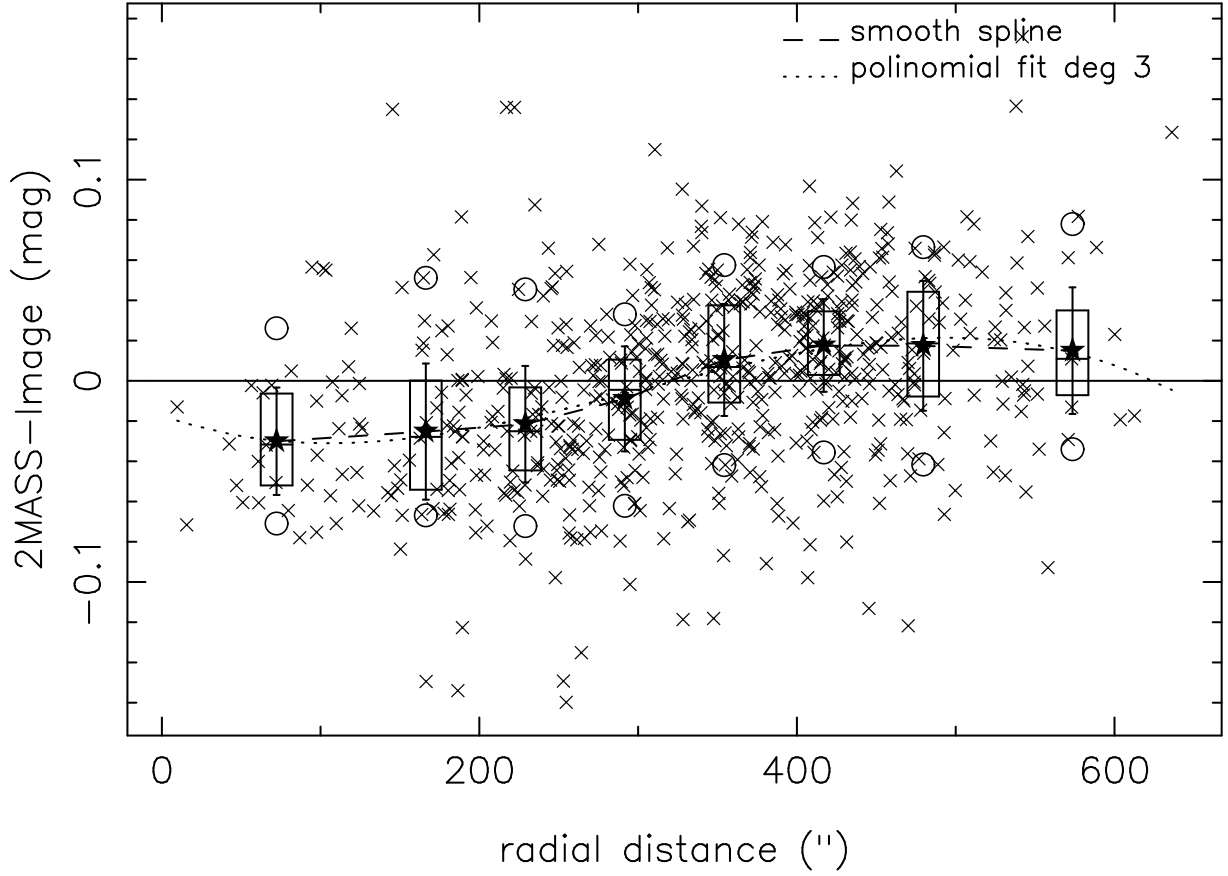


Fig. 4.— Differences between 2MASS and ALHAMBRA photometry versus the distance to the nominal pointing center in the J band. 16 pointings have been combined and a binning have been performed in the x-axis to increase the signal. For each bin the boxplot shows the mean (*stars*), the median, 1st and 3rd quartile (*boxes*), the minimum and maximum (*circles*), values after trimming the 10% on either side of the sample in each bin. The error bars represent the  $1\sigma$  interval.

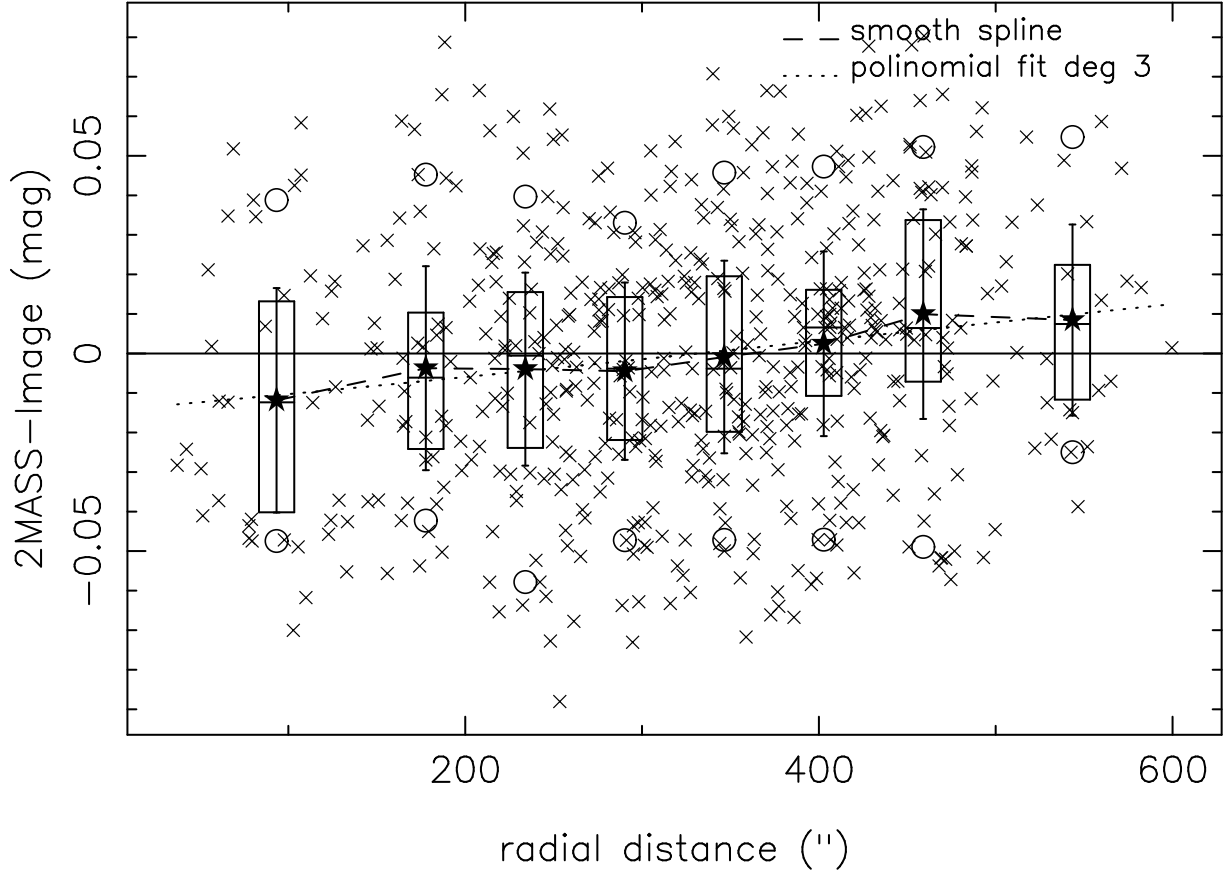


Fig. 5.— Differences between 2MASS and ALHAMBRA photometry versus the distance to the nominal pointing center after applying the pupil ghost correction in the flat-field as explained in the text. Symbols as in Fig. 4. Note that the scale in the y-axis has change with respect to Fig. 4.

for a description of how these values were obtained).

For the simulations, bright sources were selected from the image in each  $R_e$  interval. These sources were artificially dimmed to the 0.5 magnitude bin under study and injected back on the image randomly. In each iteration 40 sources were simulated, computing the recovering fraction and the robust mean (trimming the 10% on either side of the distribution) of the SExtractor desired output parameters differences between the dimmed input sources and the recovered ones. Using 9 of these iterations in each magnitude bin, we estimated the mean and rms of the recovered fraction, and SExtractor parameters differences over all the meaningful magnitude range. In Fig. 7 the completeness correction for the three  $R_e$  ranges is shown for one of the pointings in the J band.

It can be argued that with that method unrealistic pseudo-artificial sources could be produced. Whereas this could be true, the goal of this procedure is to parameterize the recovering efficiency on the basis of the source and image characteristics without any physical consideration, which will be implicitly taken into account when performing the corrections on the real data. As a validation of the procedure, the same simulations have been performed using real NICMOS F110W sources from the HDF-S Flanking Fields. The NICMOS images were resampled and convolved with a suitable Gaussian kernel to match the pixel scale and FWHM of the OMEGA2000 image under study. Initial sources were taken in the interval  $[m-1, m+1]$  (being  $m$  the magnitude under study), which produces a realistic  $mag - R_e$  relation. As can be seen from the Fig. 7 the results in the completeness correction are the same that using dimmed sources from the image.

In the top panel of Fig. 8 we show the depth to the 50% and 80% of recovering efficiency, computed using a linear interpolation in the magnitude vs. efficiency data. The figure indicates that a decreasing of the detection thresholds, in order to get a fainter level at the 50% of recovery efficiency limit, will not improve by much the limit at the 80% of completeness, which seems to reach a plateau. Moreover, as will be seen from the reliability plots, it produces a significant increase of detected spurious sources, as we explain below.

### 3.2. Detection reliability

To accurately compute the galaxy number counts it is important to establish the reliability of the detections at the faint magnitude end. To find out the optimum way to evaluate that reliability we have studied the performance of three different methods. The first approach was to create artificial sky images with the same rms and background distribution than the real ones. The ratio of spurious versus real detections was computed running

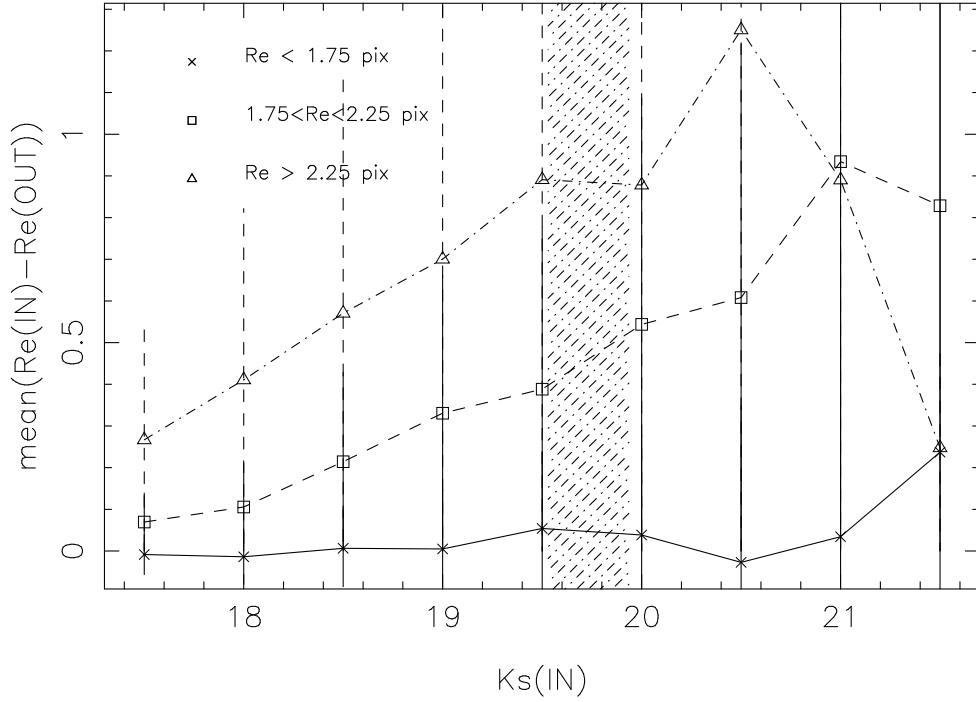
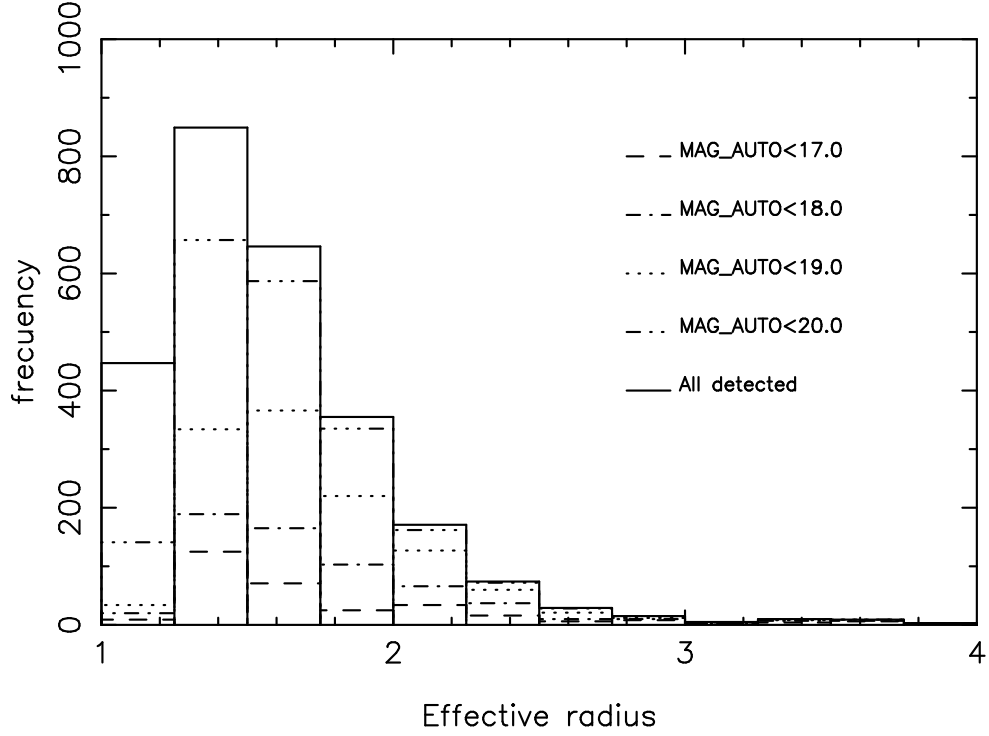


Fig. 6.— (*Top panel*) Histogram of Re for the sources in one of the pointings of the field ALH08 (*Bottom panel*) Differences between Re(in) and Re(out) for the dimmed injected sources. The symbols correspond to  $\times$   $\text{Re(in)} \leq 1.75$  pixels,  $\square$   $1.75 < \text{Re(in)} \leq 2.25$  and  $\triangle$   $\text{Re(in)} > 2.25$  pixels. The shaded is the range of magnitudes between the 50% and the 80% of detection efficiency.

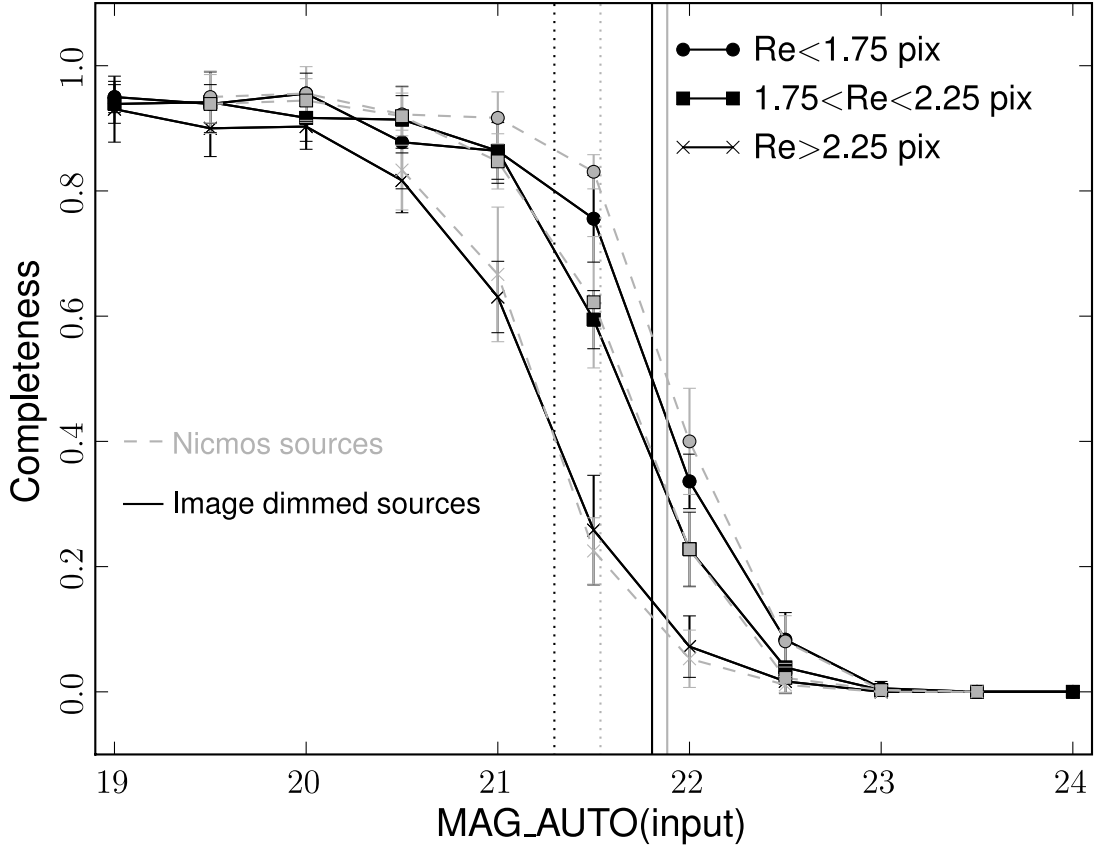


Fig. 7.— Completeness correction for the same pointing of the previous figures in the J band using  $0.8\sigma$  DETECT\_THRESH and the 2.5 pixel gaussian kernel. The vertical dotted (solid) lines are the magnitude at the 50% (80%) of detection efficiency.

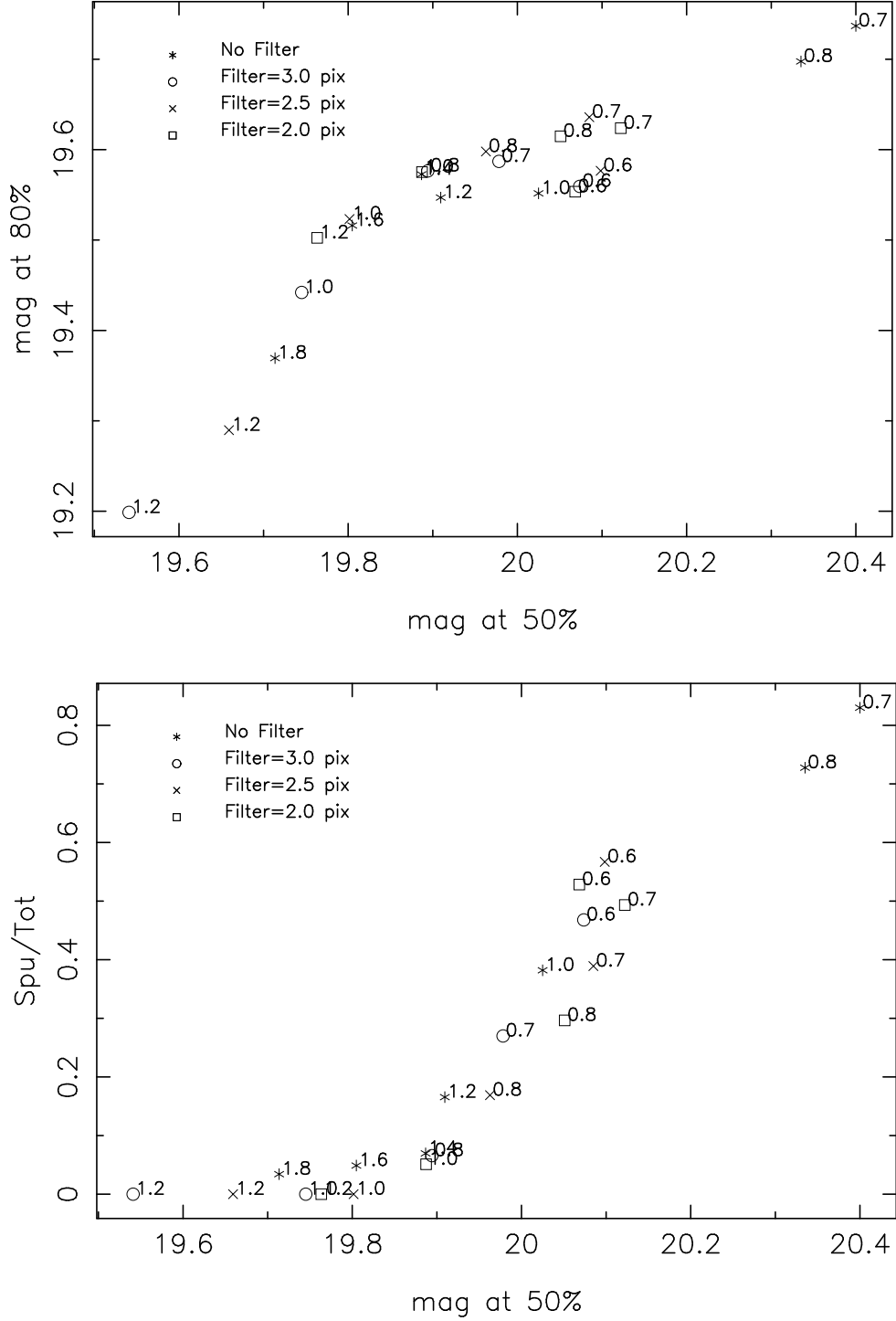


Fig. 8.— (*Top panel*) 50% vs. 80% of recovering efficiency for the same pointing as before in Ks band using different SExtractor detection strategies. The size in pixels of the SExtractor Gaussian convolution kernel is given in the labels. The detection thresholds are indicated at the points. (*Bottom panel*) 50% of detection efficiency vs. spurious to total ratio.



SExtractor over the science and the artificial sky images.

We have also inspected the performance of the method used in Cristóbal-Hornillos et al. (2003). Basically half exposure time images were created from two complementary sets of the data. The detections were performed in the total time image and the source fluxes measured in the half time images using the SExtractor double image mode for the same automatic apertures. Those created sources showing a magnitude difference greater than  $3\sigma$  were considered spurious.

The last method and the one that, at the end, produces the best results, consisted in constructing sky images using a similar combination procedure that the used to create the science images: combining the unregistered processed images with subtracted background using an artificial dither pattern. The major difficulty here was to remove the extended sources that could bias the sky even when doing trimmed mean (discarding 20% of the pixels at each side). We have confirmed that SExtractor does locate these smooth deviations over the sky rms when filtering is used. To avoid this we multiplied those sky images by -1 and used them as real sky images.

In the Fig. 9 we show a comparison between the spurious rate at the 50% of detection efficiency computed over the 'real sky' and the artificial sky. A good agreement between both methods is observed, indicating that the use of artificial images to compute the ratio of spurious to total detections is adequate. Being artificial images faster to construct we made use of them to estimate the detection reliability in each pointing.

The bottom panel of Fig. 8 shows the magnitude reached at the 50% of detection efficiency versus the spurious to total ratio at the same magnitude bin. From the figure we can see that in order to reach a deep 50% detection limiting magnitude, maintaining at the same time the number of spurious detections below 20%, the optimum SExtractor DETECT\_THRESH-FILTER combinations are: DETECT\_THRESH=1.2 or 1.4 without filtering, or DETECT\_THRESH=0.8 using a filtering with a Gaussian kernel of size similar to the image FWHM. In the top panel of Fig. 8 it is shown that those combinations reach roughly the same magnitude at the 80% of recovery efficiency. We have decided to use the latter filter-DETECT\_THRESH combination because, as can be outlined from the bottom panel in Fig. 10, the differences between the input and the recovered AUTO magnitudes in the simulations are close to zero in all the magnitude range up to the magnitude at the 80% of recovery efficiency. Close to the magnitude at the 50% of completeness the recovered magnitude appears to be  $\sim 0.1 - 0.2$  mag brighter than in the previous bin. This effect could be due to the fact than only those sources that suffer from noise brightening were found by SExtractor and used to compute the input-output magnitude differences, producing a bias towards brighter recovered objects. Following those results, the number counts in the

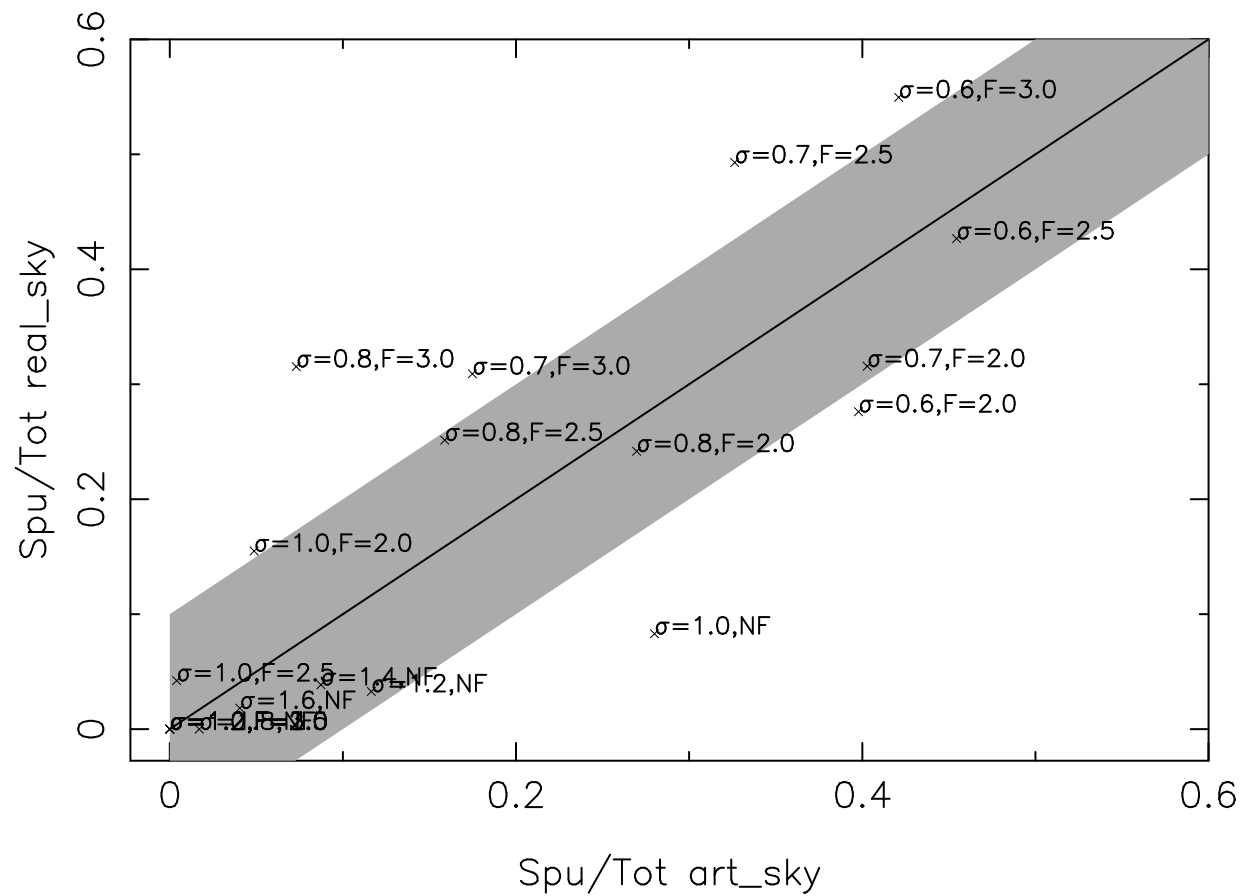


Fig. 9.— Ratio of spurious to total detections when artificial and real sky images (see text) were used. Different SExtractor DETECT\_THRESH ( $\sigma$ ) and FILTER (F) combinations are shown. The grey area corresponds to a difference less than 0.1.

following sections will be computed and corrected up to the magnitude of 80% of recovery efficiency for point-like sources, avoiding any possible systematics due to a magnitude shift at the 50% completeness bin.

As pointed before, the photometry of the sources was obtained using MAG\_AUTO. Simulations indicate no significant differences between simulated and recovered magnitudes (at the 80% recovery efficiency) for the used values of the SExtractor parameters FILTER and DETECT\_THRESH. Using the same kind of simulations we computed the rms of the recovered MAG\_AUTO values in each bin to characterize the photometric error, the results are shown in Fig. 11.

### 3.3. Star-galaxy separation

In Cristóbal-Hornillos et al. (2003) it was shown that fainter than  $K_s=17.0$  the correction due to stars is  $< 0.06$  dex. However, given the lower Galactic latitude of the ALH08 field, a higher number of contaminating stars is expected. A correct star subtraction is relevant in the intermediate magnitude range. At bright magnitudes stars can be easily separated from galaxies using a compactness criteria. In contrast, at intermediate magnitudes the star/galaxy separation is more demanding because many galaxies are barely resolved with small apparent sizes compared with the FWHM and pixel resolution, as can be seen from the diagram shown in Fig. 12.

The viability of star/galaxy separation using the SExtractor neural network has also been analyzed. For this purpose, using the same Monte Carlo method explained before, bright stars and galaxies from the images have been artificially dimmed to each magnitude bin and their SExtractor stellarity parameter recovered. In Fig. 13 it clearly appears how, in one final frame with FWHM=1.1, the input and recovered CLASS\_STAR differences are less than 0.1 up to  $K_s=18.0$ . But, in the next bin  $K_s > 18.5$ , the CLASS\_STAR of the dimmed stars and galaxies could lead to some misclassification. Nevertheless, as can be seen from the histogram in the bottom panel of Fig. 13, a non negligible number of objects start to populate the range from 0.4 to 0.8 in CLASS\_STAR at magnitudes fainter than 17 in  $K_s$ , and the selection of the CLASS\_STAR cut off might bias the star counts estimates.

An alternative way to perform the star/galaxy separation makes use simply of color-color diagrams. Huang et al. (1997) have established a reliable star/galaxy separation using the B-I vs I-K colors. Here we make use of the SDSS DR5 data for the ALH08 field to proceed with this separation using the g-r vs J- $K_s$  colors shown in Fig. 14. The star counts are corrected by the ratio of the Sloan/Alhambra completeness factors in the corresponding filter shown in

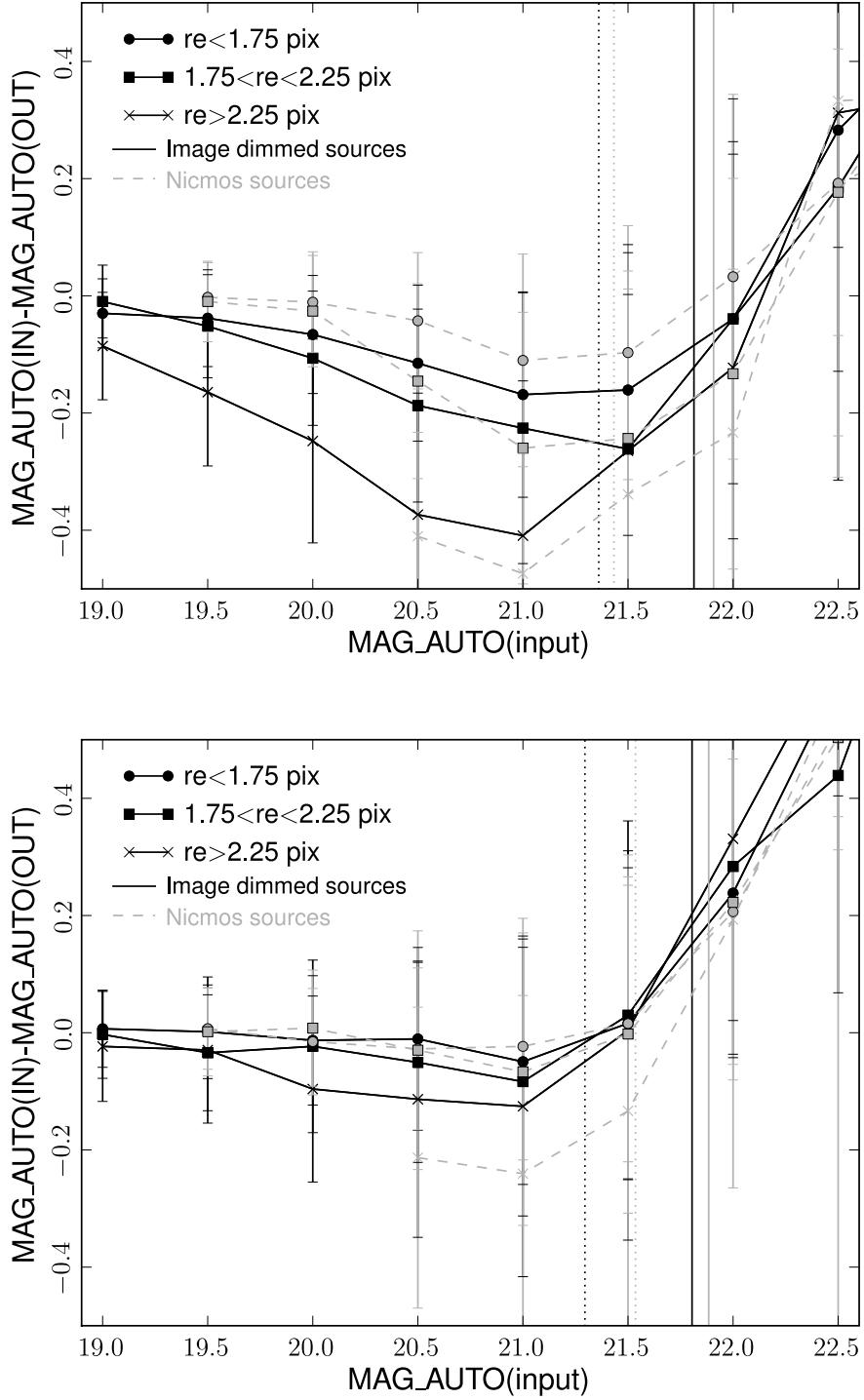


Fig. 10.— Differences between the input and the SExtractor recovered AUTO magnitudes in one of the pointings of ALH08 in the J band for two SExtractor FILTER and DETECT\_THRESH combinations: no filtering and DETECT\_THRESH=1.2 (*upper panel*), and 2.5 pixel filtering and DETECT\_THRESH=0.8 (*bottom panel*). The vertical dotted (solid) lines are the magnitude at the 50% (80%) of detection efficiency.

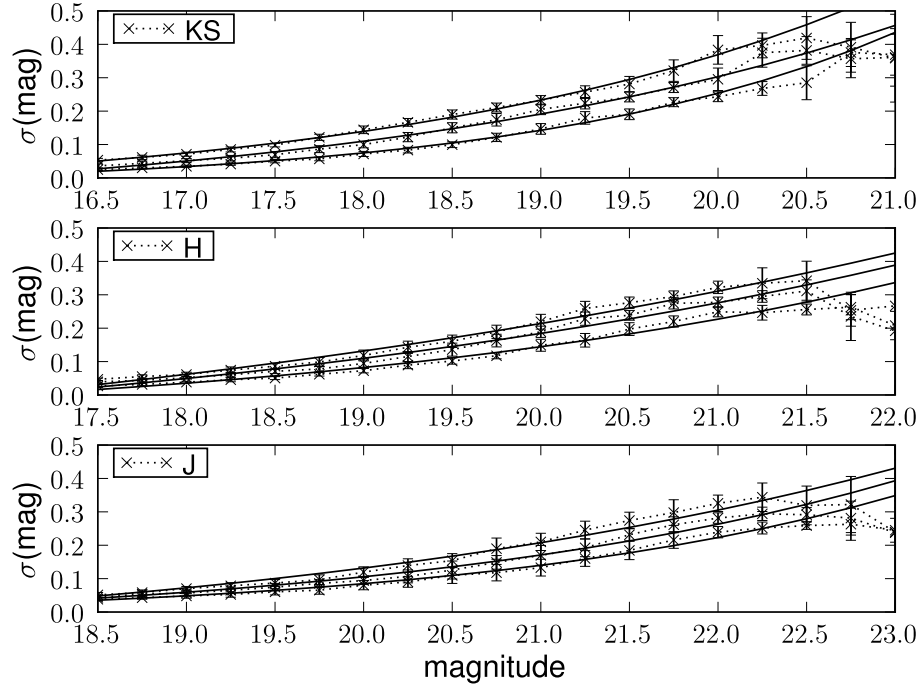


Fig. 11.— Median photometric random errors in magnitudes per magnitude bin ( $\sigma_m$ ) in the three NIR filters for the eight ALH08 pointings (*crosses and dotted lines*), the three lines represent sources with  $Re \leq 1.75$ ,  $1.75 < Re \leq 2.25$ , and  $Re > 2.25$  pixels. The magnitude errors are computed as the rms of the recovered sources magnitudes in each bin of the simulations described in the text. Error bars represent the rms of the computed  $\sigma_m$  among the pointings. Exponential grow fit ( $\sigma(m) = \sigma_0 + a \exp[b(m - m_0)]$ ) to the magnitude errors in each band (*solid lines*).

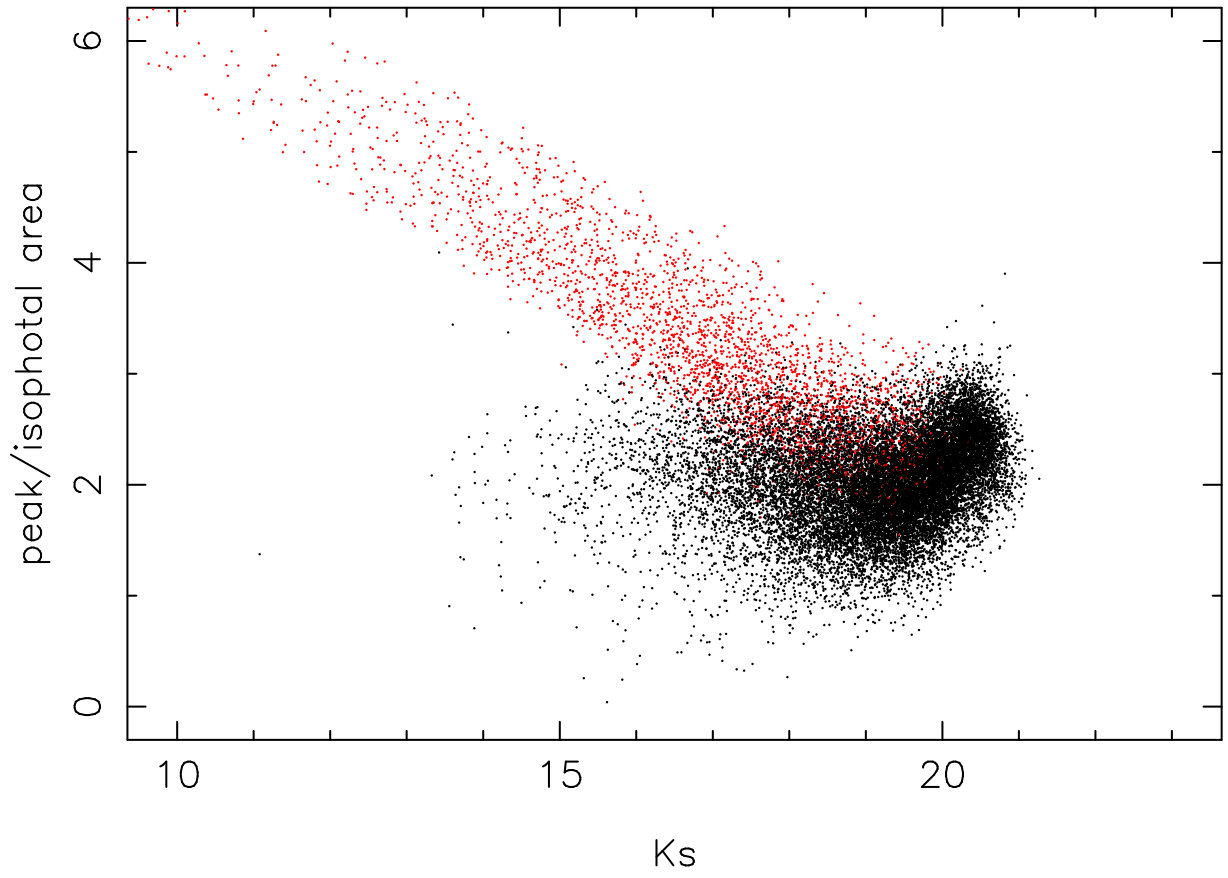


Fig. 12.— Peak/ISOPHOTAL\_AREA vs. Ks diagram. The red dots are object for which the SExtractor stellarity index is  $>0.8$ .

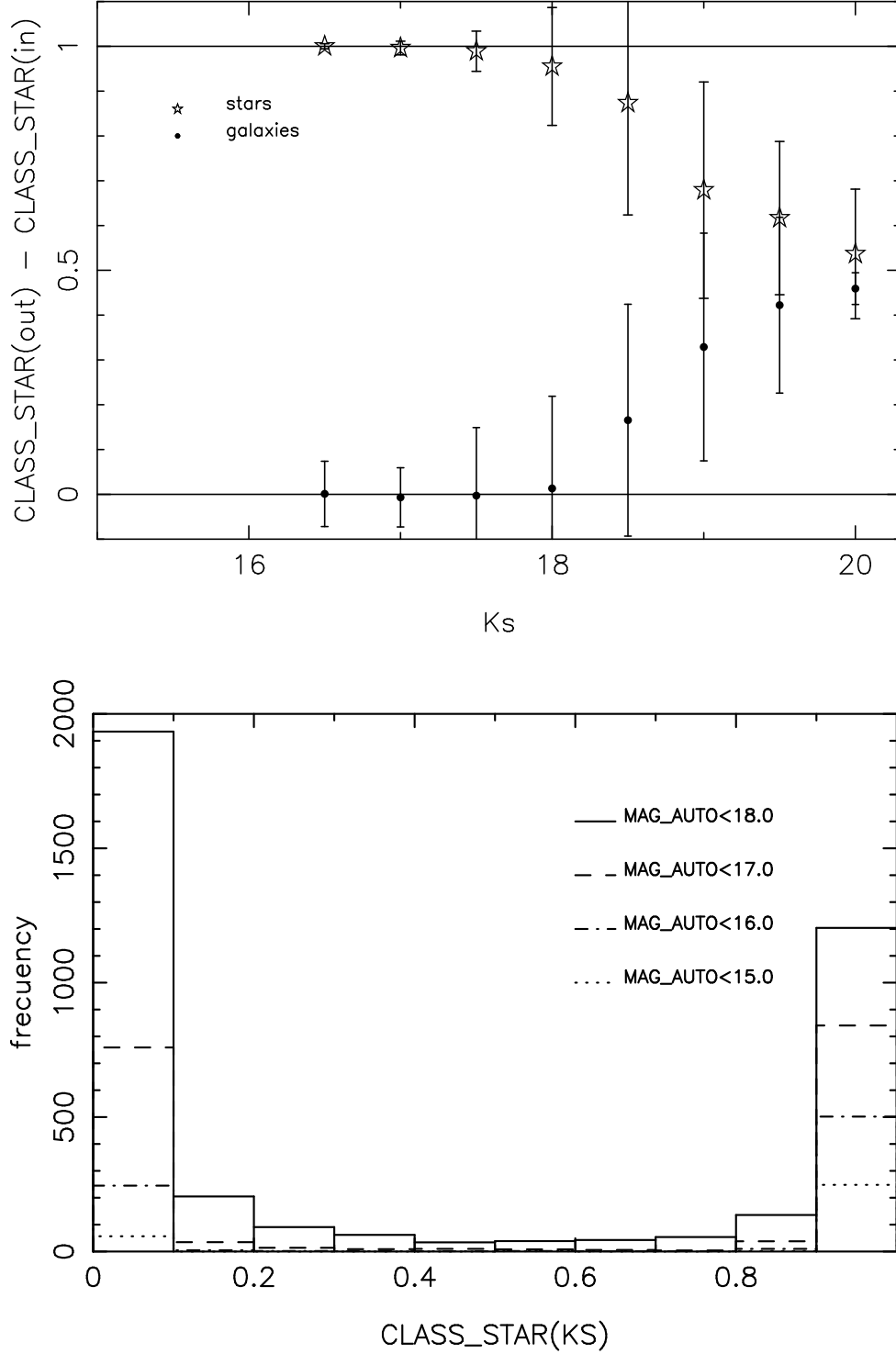


Fig. 13.— (*Top panel*)  $\text{CLASS\_STAR}$  input-output differences as a function of input artificially dimmed magnitude for a set of well defined stars ( $\text{CLASS\_STAR(in)} \sim 1$ ) and galaxies ( $\text{CLASS\_STAR(in)} \sim 0$ ). In the case of stars  $1 - (\text{CLASS\_STAR(out)} - \text{CLASS\_STAR(in)})$  is plotted. (*Bottom panel*) Histogram of  $\text{CLASS\_STAR}$  for different ranges in the  $K_s$  magnitudes.

Fig. 15. The star counts using Sloan-Alhambra colors were computed to magnitude 19.5, 18.5 and 18.0 respectively in the J, H and Ks band, where the Sloan/Alhambra completeness is  $>0.5$ . For the fainter star counts we used a 0-slope extrapolation where the models of star counts in the Galaxy are flatter (see Fig. 16). In Fig. 15 bottom panel, the correction to the  $\log(N)$  galaxy counts is presented, showing that fainter than the magnitudes up to where the color-color separation could be performed the correction in the three bands is  $< 0.08$  dex.

To check the validity of the star counts computed using the color-color approach, in Fig. 16 those are compared with the Robin et al. (1996) Galactic star counts models. The lines correspond to star counts in the Galaxy for galactic coordinates ( $l=100, b=-45$ ), very close to the coordinates of the Alhambra-08 field ( $l=99, b=-44$ ). From this figure it appears that it is possible to accurately remove the stars from the galaxy counts using the color-color diagram. This was the method we have finally used to do the star/galaxy separation.

Finally is noteworthy to mention that, star/galaxy separation will be done more accurately when the photometry in the 23 Alhambra bands is available, as the system will provide a sort of low resolution spectroscopy for each object.

#### 4. Results

The corrected galaxy number counts have been computed for the ALH08 field in the three standard NIR filters in a consistent way in the sense that they have been estimated following the same scheme for the three bands. The number count data, computed and corrected up to the magnitude of 80% of recovery efficiency for point-like sources, are presented in the Tabs. 1, 2 and 3.

The error in the number counts for each pointings are the sum in quadrature of the rms in the estimation of the completeness corrections, with the contribution of Poisson noise and galaxy clustering calculated for each magnitude bin following eq. 1 (Huang et al. 1997), that includes the angular correlation function.

$$\sigma_i^2 = N_i(m) + 5.3 \left( \frac{r_0}{r_\star} \right) \Omega_i^{(1-\gamma)/2} N_i^2(m) \quad (1)$$

being  $N_i$  the raw counts in the pointing,  $r_0 = 7.1$  Mpc,  $\gamma = 1.77$  and  $5 \log(r_\star) = m - M_\star - 25$ .  $M_\star$  is set to -22.95, -23.69 and -23.93 for the J, H and Ks filters. The final uncertainty in the combined counts per square degree and magnitude is given by:



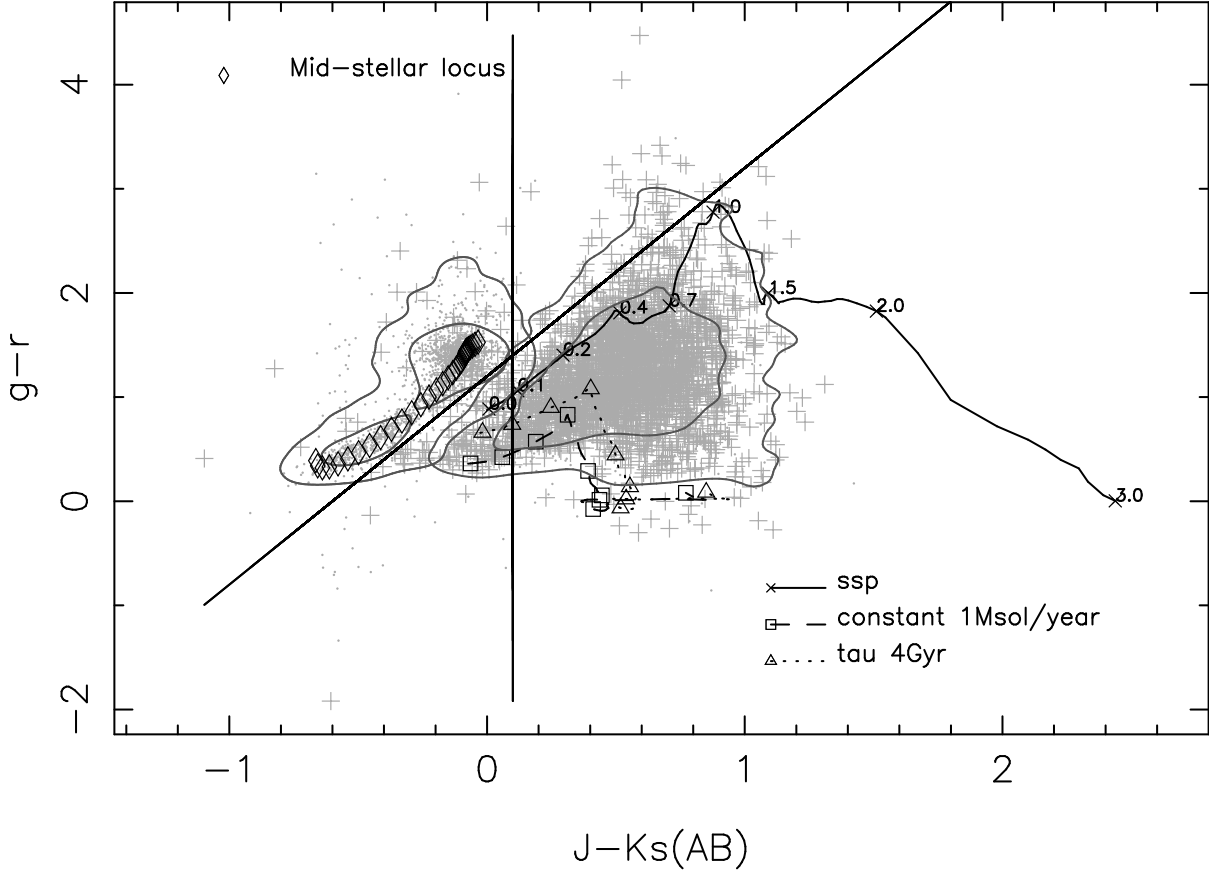


Fig. 14.—  $g-r$  vs  $J-Ks$  plot used to perform the star-galaxy separation. All objects in ALH08 with  $S/N > 5$  are plotted. The line separating the two classes is  $g-r = 1.2 + 2.0 \cdot (J-Ks)_{AB}$ . The plotted symbols correspond to the Sloan classification *dots* for representing stars and the *crosses* for galaxies. Redshift-color tracks for three galaxy models constructed using the Bruzual & Charlot (2003) code are shown. The redshift values are displayed over the Single Stellar Population (SSP) track, the marks over the other 2 curves have the same redshift spacing. The *diamonds* represent the mid stellar locus given in Covey et al. (2007). Two contour lines containing the 95% and the 68% are displayed for the galaxies and stars using the Sloan classification.

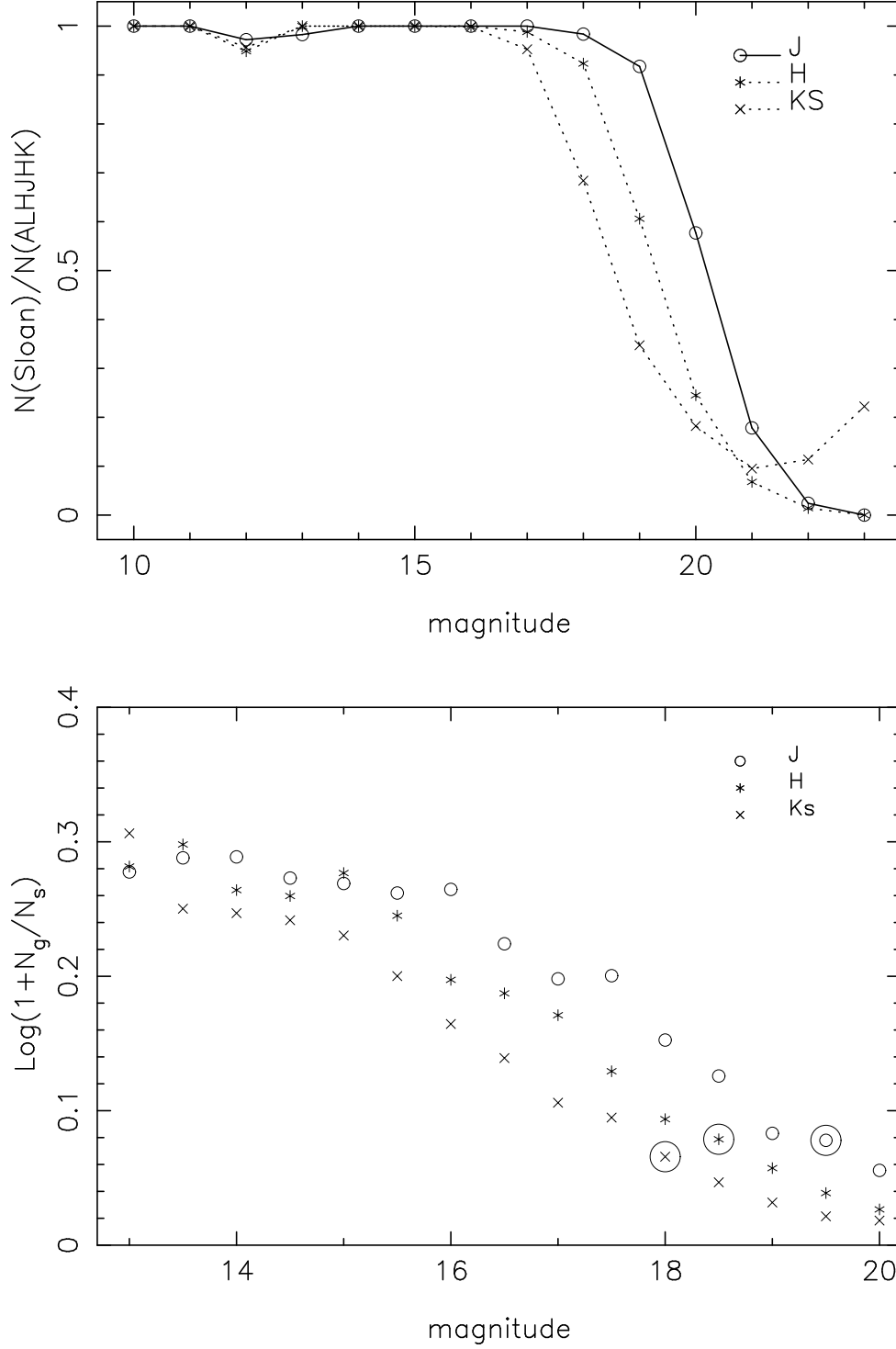


Fig. 15.— (*Top panel*) The ratio of sources identified in the Alhambra field for which there is a counterpart in the Sloan SDSS DR5 catalog. (*Bottom panel*) The correction subtracted from  $\log(N)$  galaxy counts due to stars. The big open circle indicates the point up to which the number of stars can be estimated from the Sloan-Alhambra colors (see text), the fainter star counts assume a flat extrapolation from this value.

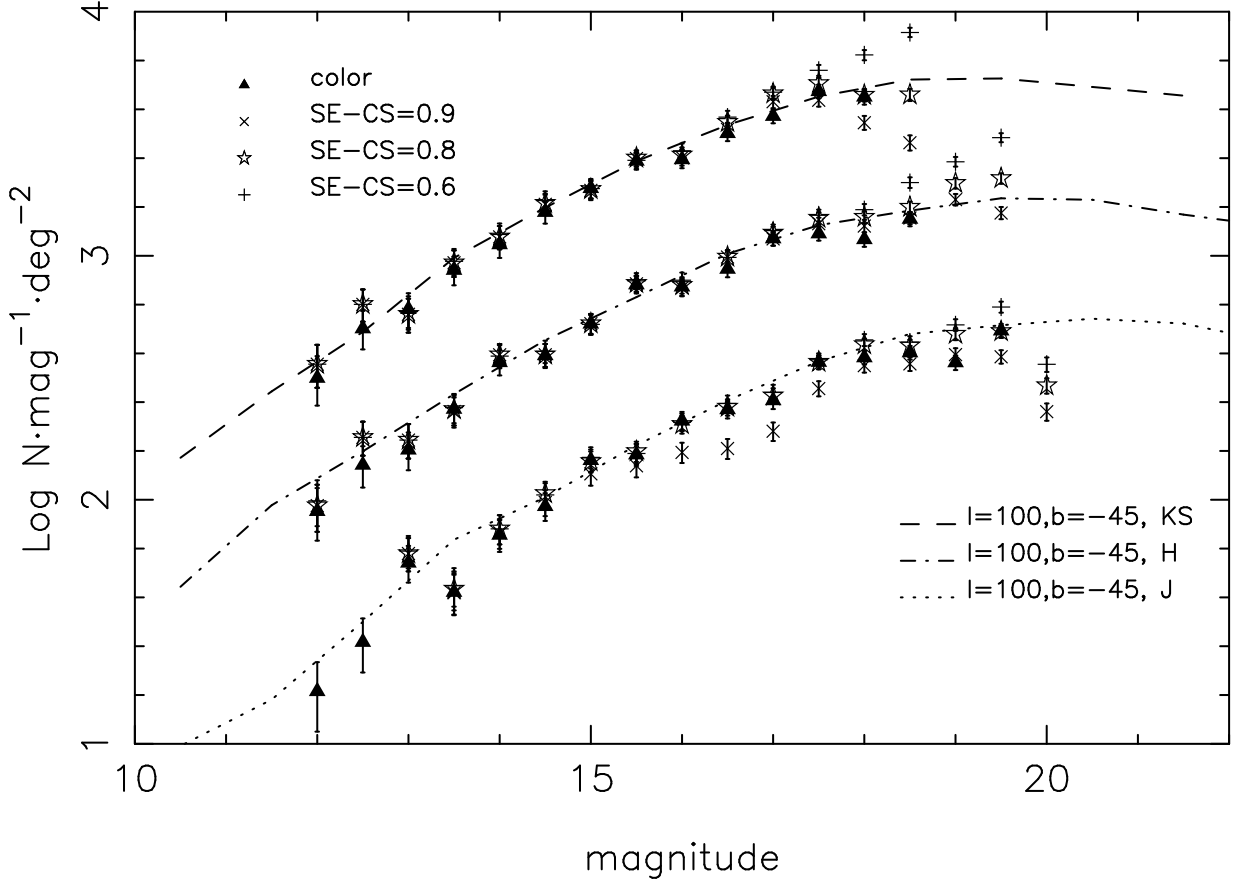


Fig. 16.— Star counts for the ALH08 field compared with the Robin et al. (1996) Galactic count model. The J and Ks data have been plotted with an offset of -0.5 and 0.5 dex in the y-axis.

$$\sigma(m) = \frac{\sqrt{\sum \sigma_i^2}}{\Omega \Delta m} \quad (2)$$

In the Figs. 17, 18, and 19 the Alhambra counts in the J,H, and Ks bands are plotted together with the computed number counts from other surveys.

Let us first point out the general aspect of those counts, leaving more detailed considerations for the next section. Our corrected J band galaxy counts are in overall agreement with those computed in other works (Teplitz et al. 1999; Feulner et al. 2007), the bright end of the results presented by Maihara et al. (2001), and the ELAIS-N2 data from Väisänen et al. (2000). Nevertheless, our counts are lower than those given by Bershadsky et al. (1998) at magnitudes  $J > 21.5$ .

The Alhambra counts in the H band are in good correspondence with the published data by Martini (2001); Frith et al. (2006) and with the bright part of the data from Moy et al. (2003), after applying an offset of -0.215 mag. This offset was calculated following the -0.065 calibration difference among Las Campanas Infrared Survey (LCIRS, Chen et al. (2002)) reported in Moy et al. (2003), and the systematic of -0.28 magnitude difference between LCIRS and 2MASS magnitudes reported in Frith et al. (2006). However, the faint end ( $H > 20$ ) of our data is significantly above the faint number count data from Yan et al. (1998) and Metcalfe et al. (2006), obtained from NICMOS observations.

Regarding the Ks filter, for which there are numerous number counts studies, our galaxy counts are in good agreement with most of the published data, as can be appreciated in the Fig. 19.

#### 4.1. The measured slopes

We have found, as in previous studies, that the slope of the galaxy number counts displays a clear change at  $Ks \sim 17.3$  (see Fig. 20). However, in the present work we also have found this change of slope in the J and H band galaxy counts at  $J \sim 19.1$  and  $H \sim 18.2$ .

The slopes of the bright end and faint end counts in the different bands were measured using the least squares method. The values that we have calculated and the magnitude ranges used for the fits are listed in Tab. 4. The results show that the faint slopes for the three NIR filters are the same within  $2\sigma$ , whereas the bright slope is steeper in the Ks band.

As is described in Teerikorpi (2004) the fact that the photometric error increases at fainter magnitudes, and that the differential galaxy number counts also rises towards lower

Table 1. Corrected galaxy number counts in the J band.

Magnitude	raw counts <sup>a</sup>	eff. cor. <sup>b</sup>	$\log(Nc)$ <sup>c</sup> $N \cdot mag^{-1} \cdot deg^{-2}$	$\log(Nm)$ <sup>d</sup> $N \cdot mag^{-1} \cdot deg^{-2}$	area $deg^2$
13.00	43.0	1.00	$1.31^{+0.49}_{-1.31}$	$1.30^{+0.73}_{-1.30}$	0.441
13.50	31.0	1.00	$0.92^{+0.73}_{-0.92}$	$0.95^{+0.96}_{-0.95}$	0.441
14.00	53.0	1.00	$1.13^{+0.66}_{-1.13}$	$1.08^{+0.90}_{-1.08}$	0.441
14.50	75.0	1.00	$1.63^{+0.36}_{-1.63}$	$1.64^{+0.61}_{-1.64}$	0.441
15.00	118.0	1.00	$1.88^{+0.28}_{-1.07}$	$1.89^{+0.49}_{-1.89}$	0.441
15.50	129.0	1.00	$2.00^{+0.23}_{-0.54}$	$2.00^{+0.41}_{-2.00}$	0.441
16.00	175.0	1.00	$2.11^{+0.22}_{-0.47}$	$2.11^{+0.34}_{-2.11}$	0.441
16.50	242.0	1.00	$2.55^{+0.10}_{-0.13}$	$2.56^{+0.24}_{-0.55}$	0.441
17.00	309.0	1.00	$2.77^{+0.07}_{-0.08}$	$2.77^{+0.15}_{-0.23}$	0.441
17.50	436.0	1.00	$2.91^{+0.06}_{-0.07}$	$2.91^{+0.09}_{-0.12}$	0.441
18.00	634.0	1.00	$3.22^{+0.04}_{-0.04}$	$3.22^{+0.11}_{-0.14}$	0.441
18.50	832.0	1.00	$3.40^{+0.03}_{-0.03}$	$3.40^{+0.09}_{-0.11}$	0.441
19.00	1128.0	1.07	$3.63^{+0.02}_{-0.02}$	$3.64^{+0.06}_{-0.07}$	0.441
19.50	1615.0	1.08	$3.80^{+0.02}_{-0.02}$	$3.80^{+0.05}_{-0.05}$	0.441
20.00	2303.0	1.09	$3.99^{+0.06}_{-0.08}$	$3.99^{+0.08}_{-0.10}$	0.441
20.50	3285.0	1.12	$4.18^{+0.04}_{-0.05}$	$4.18^{+0.06}_{-0.07}$	0.441
21.00	4455.0	1.17	$4.34^{+0.03}_{-0.03}$	$4.34^{+0.05}_{-0.05}$	0.441
21.50	5030.0	1.25	$4.50^{+0.02}_{-0.03}$	$4.50^{+0.03}_{-0.03}$	0.381
22.00	1739.0	1.52	$4.67^{+0.03}_{-0.03}$	$4.67^{+0.01}_{-0.02}$	0.109

<sup>a</sup>Raw counts including stars.

<sup>b</sup>Effective correction, defined as  $(Nc + Nst)/(2 \cdot area \cdot raw)$ .

<sup>c</sup>Corrected galaxy counts, errors corresponds to the Poissonian and galaxy clustering uncertainty plus error in completeness added in quadrature.

<sup>d</sup>Mean of the 8 pointings and its rms.

Table 2. Corrected galaxy number counts in the H band.

Magnitude	raw counts <sup>a</sup>	eff. cor. <sup>b</sup>	$\log(Nc)$ <sup>c</sup> $N \cdot mag^{-1} \cdot deg^{-2}$	$\log(Nm)$ <sup>d</sup> $N \cdot mag^{-1} \cdot deg^{-2}$	area $deg^2$
12.00	22.0	1.00	$0.97^{+0.64}_{-0.97}$	$0.98^{+0.98}_{-0.98}$	0.444
12.50	40.0	1.00	$1.62^{+0.30}_{-1.62}$	$1.60^{+0.47}_{-1.60}$	0.444
13.00	39.0	1.00	$1.19^{+0.56}_{-1.19}$	$1.19^{+0.79}_{-1.19}$	0.444
13.50	53.0	1.00	$0.52^{+1.19}_{-0.52}$	$0.55^{+1.44}_{-0.55}$	0.444
14.00	97.0	1.00	$1.85^{+0.28}_{-0.95}$	$1.86^{+0.49}_{-1.86}$	0.444
14.50	106.0	1.00	$1.94^{+0.24}_{-0.61}$	$1.94^{+0.54}_{-1.94}$	0.444
15.00	131.0	1.00	$1.81^{+0.33}_{-1.81}$	$1.81^{+0.59}_{-1.81}$	0.444
15.50	223.0	1.00	$2.39^{+0.14}_{-0.21}$	$2.39^{+0.25}_{-0.63}$	0.444
16.00	288.0	1.00	$2.74^{+0.07}_{-0.09}$	$2.74^{+0.16}_{-0.25}$	0.444
16.50	363.0	1.00	$2.88^{+0.06}_{-0.07}$	$2.88^{+0.12}_{-0.17}$	0.444
17.00	541.0	1.00	$3.10^{+0.04}_{-0.05}$	$3.10^{+0.06}_{-0.07}$	0.444
17.50	788.0	1.00	$3.37^{+0.03}_{-0.03}$	$3.37^{+0.10}_{-0.14}$	0.444
18.00	1074.0	1.00	$3.56^{+0.02}_{-0.02}$	$3.57^{+0.06}_{-0.07}$	0.444
18.50	1512.0	1.05	$3.76^{+0.02}_{-0.02}$	$3.76^{+0.06}_{-0.07}$	0.444
19.00	2110.0	1.05	$3.94^{+0.07}_{-0.08}$	$3.94^{+0.08}_{-0.10}$	0.444
19.50	3138.0	1.07	$4.14^{+0.04}_{-0.05}$	$4.14^{+0.05}_{-0.06}$	0.444
20.00	4456.0	1.12	$4.32^{+0.03}_{-0.03}$	$4.32^{+0.04}_{-0.05}$	0.444
20.50	5879.0	1.23	$4.49^{+0.02}_{-0.02}$	$4.49^{+0.04}_{-0.05}$	0.444
21.00	2578.0	1.48	$4.65^{+0.02}_{-0.02}$	$4.65^{+0.02}_{-0.02}$	0.165

<sup>a</sup>Raw counts including stars.

<sup>b</sup>Effective correction, defined as  $(Nc + Nst)/(2 \cdot area \cdot raw)$ .

<sup>c</sup>Corrected galaxy counts, errors corresponds to the Poissonian and galaxy clustering uncertainty plus error in completeness added in quadrature.

<sup>d</sup>Mean of the 8 pointings and its rms.

Table 3. Corrected galaxy number counts in the Ks band.

Magnitude	raw counts <sup>a</sup>	eff. cor. <sup>b</sup>	$\log(Nc)$ <sup>c</sup> $N \cdot mag^{-1} \cdot deg^{-2}$	$\log(Nm)$ <sup>d</sup> $N \cdot mag^{-1} \cdot deg^{-2}$	area $deg^2$
12.00	25.0	1.00	$1.14^{+0.54}_{-1.14}$	$1.13^{+0.74}_{-1.13}$	0.440
12.50	44.0	1.00	$1.61^{+0.32}_{-1.61}$	$1.60^{+0.52}_{-1.60}$	0.440
13.00	41.0	1.00	...	...	0.440
13.50	78.0	1.00	$1.89^{+0.24}_{-0.55}$	$1.90^{+0.32}_{-1.90}$	0.440
14.00	101.0	1.00	$2.03^{+0.20}_{-0.39}$	$2.03^{+0.47}_{-2.03}$	0.440
14.50	141.0	1.00	$2.21^{+0.16}_{-0.26}$	$2.22^{+0.32}_{-2.22}$	0.440
15.00	188.0	1.00	$2.41^{+0.12}_{-0.17}$	$2.41^{+0.26}_{-0.73}$	0.440
15.50	291.0	1.00	$2.74^{+0.07}_{-0.09}$	$2.74^{+0.14}_{-0.21}$	0.440
16.00	375.0	1.00	$2.96^{+0.05}_{-0.06}$	$2.96^{+0.11}_{-0.15}$	0.440
16.50	585.0	1.00	$3.22^{+0.03}_{-0.04}$	$3.22^{+0.08}_{-0.09}$	0.440
17.00	940.0	1.00	$3.49^{+0.02}_{-0.02}$	$3.49^{+0.06}_{-0.07}$	0.440
17.50	1307.0	1.03	$3.67^{+0.02}_{-0.02}$	$3.67^{+0.05}_{-0.06}$	0.440
18.00	1836.0	1.04	$3.86^{+0.01}_{-0.02}$	$3.86^{+0.06}_{-0.07}$	0.440
18.50	2614.0	1.05	$4.04^{+0.05}_{-0.06}$	$4.04^{+0.07}_{-0.08}$	0.440
19.00	3698.0	1.11	$4.24^{+0.04}_{-0.04}$	$4.24^{+0.06}_{-0.07}$	0.440
19.50	4477.0	1.37	$4.42^{+0.03}_{-0.03}$	$4.42^{+0.04}_{-0.04}$	0.440
20.00	574.0	1.55	$4.50^{+0.04}_{-0.05}$	$4.50^{+0.02}_{-0.02}$	0.054

<sup>a</sup>Raw counts including stars.

<sup>b</sup>Effective correction, defined as  $(Nc + Nst)/(2 \cdot area \cdot raw)$ .

<sup>c</sup>Corrected galaxy counts, errors corresponds to the Poissonian and galaxy clustering uncertainty plus error in completeness added in quadrature.

<sup>d</sup>Mean of the 8 pointings and its rms.

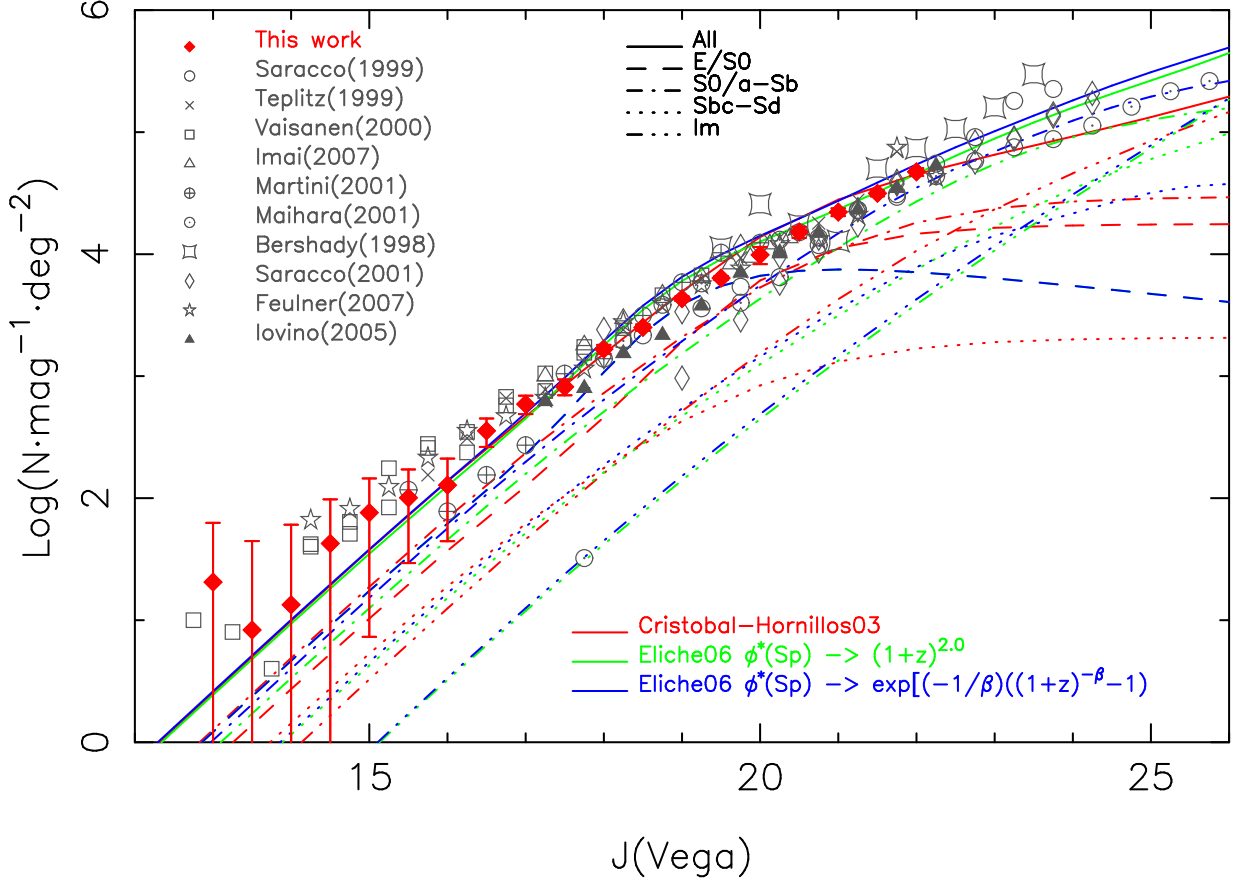


Fig. 17.— Galaxy number counts in the J filter compared with data from other surveys. The lines correspond to the number counts models in Cristóbal-Hornillos et al. (2003) and Eliche-Moral et al. (2006) described in the text.



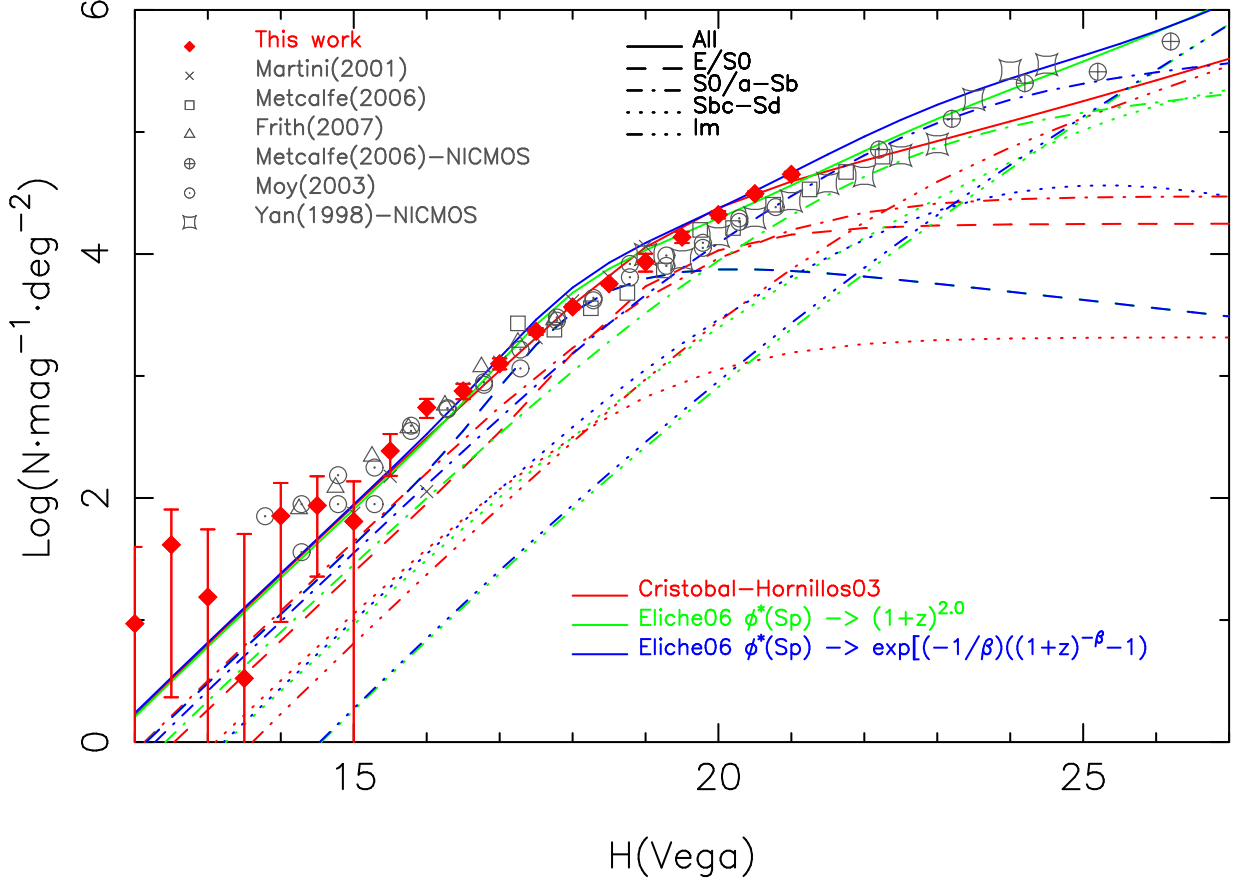


Fig. 18.— Galaxy number counts in the H filter compared with data from other surveys and the models in Cristóbal-Hornillos et al. (2003) and Eliche-Moral et al. (2006) described in the text.

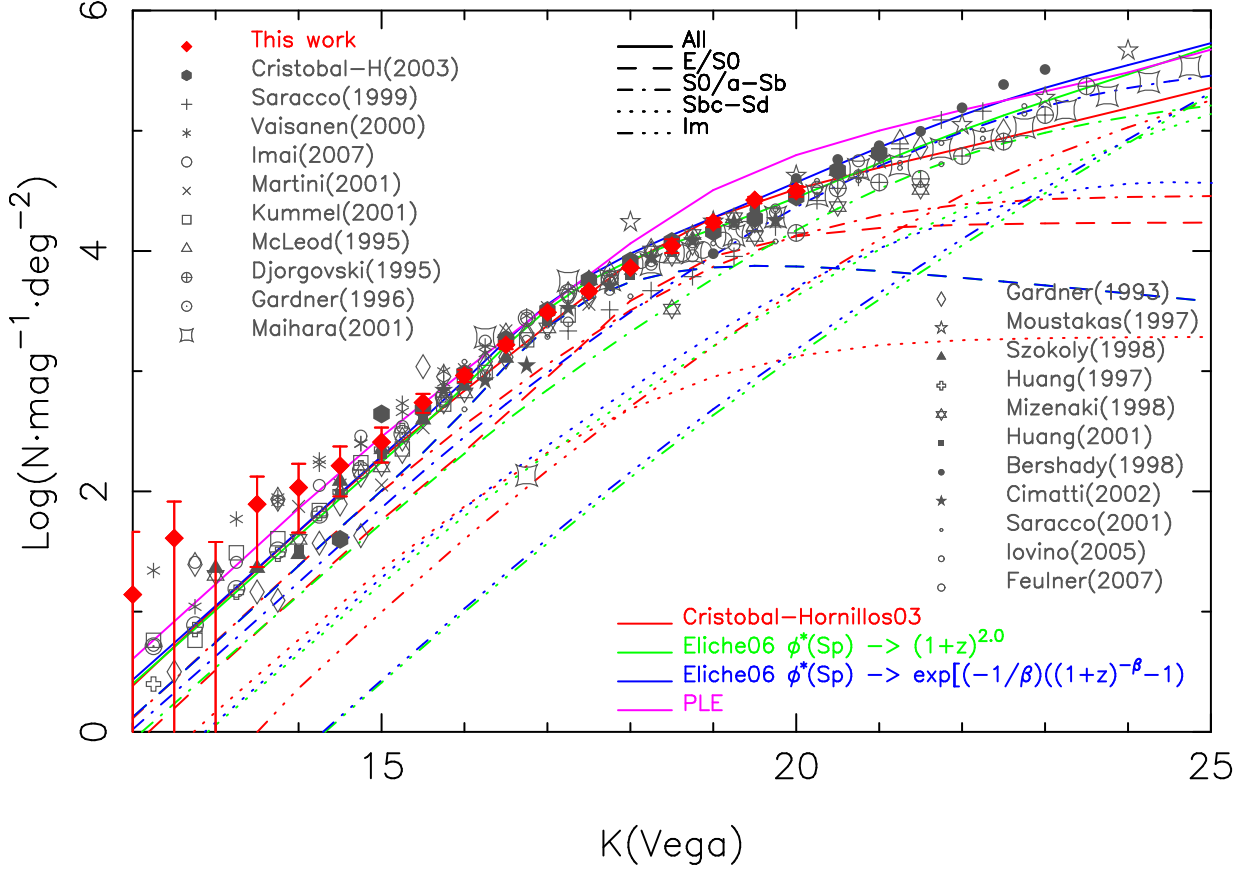


Fig. 19.— Galaxy number counts in the Ks filter compared with data from the literature and the galaxy counts models in Cristóbal-Hornillos et al. (2003) Eliche-Moral et al. (2006) described in the text. Also it is shown a model where only the passive evolution of stellar populations is considered (PLE).

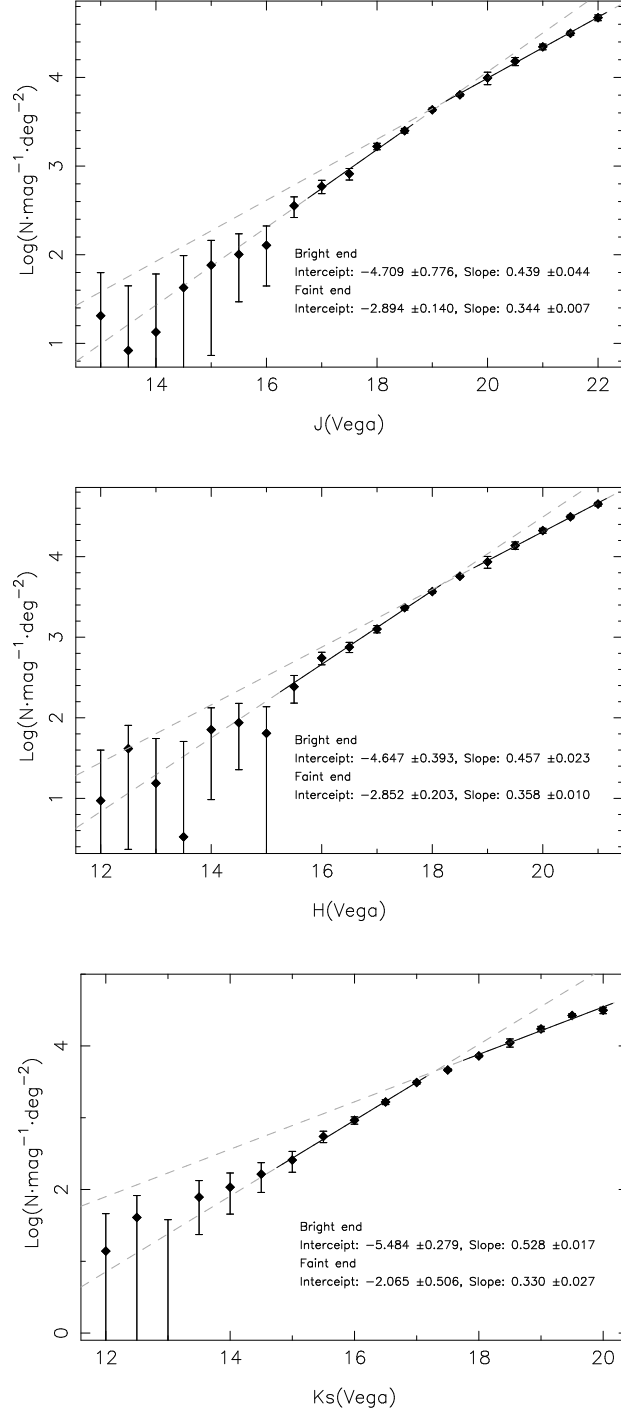


Fig. 20.— Galaxy number count bright and faint slopes found in this work. Error bars are the Poissonian and galaxy clustering uncertainty added in quadrature with the rms in the estimation of the completeness corrections.

fluxes, lead to a stepper observed slope at the faint end. This effect is related with the Eddington bias (Eddington 1913). To investigate if the computed magnitude errors could bias our slope estimates we have done the following study. First, in each filter we use the exponential grow function fit to the magnitude errors (Fig. 11). Then we extended our computed number counts one magnitude fainter using the corresponding slope in Tab. 4, simulating a Gaussian decay for fainter magnitudes. The parameter  $\sigma$  for the Gaussian is the value of the exponential fit to the error values for point-like sources at one magnitude fainter than the last bin given in Tabs. 1, 2 and 3 ( $\sigma = 0.35, 0.41$  and  $0.44$  at respectively J=23.0, H=22.0 and Ks=21.0). Using the fitted magnitude errors for point-like objects ( $\sigma(m)$ ), and assuming that real distribution is close to the extended number counts ( $N(m)$ ), we simulate the bias produced by the photometric error on the observed counts, by convolving the  $N(m)$  with  $\sigma(m)$  using the eq. 3. The results indicate an increase in the slope less than 0.015 in the case of J and H filters, and 0.03 in the Ks band, meaning that the original distributions would have a faint end slope of 0.33, 0.34 and 0.30 in the J, H, and Ks filters in the ranges given in Tab. 4.

$$N(m_{obs}) = \int N(m) \frac{1}{\sqrt{2\pi}\sigma} e^{-\frac{(m-m_{obs})^2}{2\sigma^2(m)}} dm \quad (3)$$

The increase of the slope is not observed when we simulate this bias directly over the observed count distribution. This is due to the fact that fainter than the 80% completeness magnitude bin there is a fast decrease of the number of detected sources, and that in this bin the typical photometric error ( $\sigma_m = 0.23 - 0.26$ ) for the dominant point-like sources, makes that the bias do not significantly affect to the previous bins. In this case the slopes after applying the bias are lower than the computed from the observed number counts ( $0.33 \pm 0.01$ ,  $0.33 \pm 0.02$ , and  $0.30 \pm 0.02$  in J, H and Ks). This result would suggest that the original distribution slopes at the faint end would be higher than the ones given in Tab. 4. We have used the combined results from this paragraph and the previous one to increase the uncertainty in the slope, leaving the values computed directly from the observed number counts as satisfactory estimates of the real distribution slope at the faint end.

Our results for the Ks band are in good agreement with other K-band surveys which also report a similar change of slope in the galaxy counts in the range 17.0-18.0 (Daddi et al. 2000; Huang et al. 2001; Cristóbal-Hornillos et al. 2003; Iovino et al. 2005). At the bright part our slopes are close to the values measured in Kümmel & Wagner (2000); Martini (2001); Cristóbal-Hornillos et al. (2003); Iovino et al. (2005) (see Tab. 5), while other references point to a steeper bright slope (Gardner et al. 1993, 1996; Huang et al. 1997, 2001). This could be due to the fact that the last authors could extend the power-law fit to brighter magnitudes due to their larger surveyed area, whereas our fit is closer to the magnitude

where the break is found which would lead to a decrease in the slope if the break transition is smooth. In the faint part of the Ks counts a slope of 0.33 found in this work is in agreement with Bershadsky et al. (1998); Huang et al. (2001); Imai et al. (2007). The value of the faint slope from the ALHAMBRA data is however steeper than the value reported in some surveys covering smaller areas, where the fitted range extends to fainter magnitudes, Gardner et al. (1993); Moustakas et al. (1997); Maihara et al. (2001). Here the differences might be due to cosmic variance. A larger than  $2\sigma$  disagreement is found with the faint slope of Cristóbal-Hornillos et al. (2003) fitted in the range [17.5,19.5], although their value increase to 0.29 when the fit interval is extended to Ks=21.0. Kümmel & Wagner (2000) give a higher value for the faint slope, however due to the brighter limiting magnitude of their number counts they could established a break or the beginning of a roll-over in the interval Ks=[16.5,17.0].

In the H and J bands there are fewer works reporting count-slope values. Our results, given in Tab. 4, show similar slopes for the J and H filter at the bright and faint ends. As can be seen in Tabs. 6 and 7 our result at the bright end are in good agreement with the bright-end slope values to H=19 given in Martini (2001) and Chen et al. (2002), and in the J filter with the results in Väisänen et al. (2000) and Iovino et al. (2005). At the faint end, only the slope values in Maihara et al. (2001) in the J filter, estimated in an area of 4 arcsec<sup>2</sup>, and Chen et al. (2002) have a significant discrepancy.

## 5. Comparison with Models of Evolution

Historically, the galaxy number counts have been used to examine parameters of the cosmological model and to test different galaxy evolution scenarios. Now that the cosmological parameters are fixed using other methods the consequences derived from the galaxy counts for the galaxy evolution have become more precise. The ALHAMBRA computed counts in the three NIR bands provide a good dataset which, when combined with other op-

Table 4. Measured slopes in the J,H and Ks filters

Filter	Bright range	Bright slope	Faint range	Faint slope
J	[17.0,18.5]	0.44±0.04	[19.5,22.0]	0.34±0.01
H	[15.5,18.0]	0.46±0.02	[19.0,21.0]	0.36±0.02
Ks	[15.0,17.0]	0.53±0.02	[18.0,20.0]	0.33±0.03

Table 5. Characteristics of the surveys in the K band

Reference	Surveyed area sqarcmin	limit magnitude	bright range	bright slope	faint range	faint slope	filter
Gardner93	5688	14.5 <sup>c</sup>	[10.0,16.0]	0.67	[18.0,23.0]	0.23	K'
Gardner93	582	16.75 <sup>c</sup>	—	—	—	—	—
Gardner93	167.7	18.75 <sup>c</sup>	—	—	—	—	—
Gardner93	16.5	22.5	—	—	—	—	—
Glazebrook94	552	16.5 <sup>c</sup>	—	—	—	—	K
Djorgovski95	3	23.5 <sup>c</sup>	—	—	[20.0,23.5]	0.32±0.02	K
McLeod95	22.5,2.0	19.5,21.25 <sup>c</sup>	—	—	—	—	Ks
Gardner96	35424	15.75 <sup>c</sup>	<16.0	0.63±0.01	—	—	K
Moustakas97	2.0	24.0 <sup>c</sup>	—	—	[18.0,23.0]	0.23±0.02	K
Huang97	29628	16.0 <sup>c</sup>	[12.0,16.0]	0.689±0.013	—	—	K'
Minezaki98	181,2.21	19.1,21.2 <sup>d</sup>	—	—	[18.25,18-75]	0.28	K'
Bershady98	1.5	24.00 <sup>b</sup>	—	—	>18.5	0.36	K
Szokoly98	2185	16.5 <sup>c</sup>	[14.5,16.5]	0.50±0.03	—	—	Ks
Saracco99	20	22.25 <sup>c</sup>	—	—	[17.25,22.5]	0.38	Ks
Väisänen00	3492,2088	16.75,17.75 <sup>c</sup>	[15.0,18.0]	0.40-0.45	—	—	K
Martini01	180,51	17.0,18.0 <sup>c</sup>	[14.0,18.0]	0.54	—	—	K
Daddi00	701,447	18.5,19.0 <sup>c</sup>	[14.0,17.5]	0.53±0.02	>17.5	0.32±0.02	Ks
Kümmel00	3348	17.25 <sup>c</sup>	[10.5,17.0]	0.56±0.01	[16.5,17.5]	0.41	K
Maihara01	4	25.25 <sup>c</sup>	—	—	>20.1	0.23	K'
Saracco01	13.6	22.75 <sup>c</sup>	—	—	>19	0.28	Ks
Huang01	720	19.5 <sup>c</sup>	<16.5	0.64	>17	0.36	K'
Cimatti02	52	19.75 <sup>c</sup>	—	—	—	—	Ks
Cristobal03	180,50	20.0,21.0 <sup>b</sup>	[15.5,17.5]	0.54	[17.5,19.5]	0.25	Ks
Iovino05	414	20.75 <sup>c</sup>	[15.75,18.0]	0.47±0.23	[18.0,21.25]	0.29±0.08	Ks
Elston06	25560	19.2 <sup>b</sup>	—	—	—	—	Ks
Imai07	750,306	18.625,19.375 <sup>c</sup>	<18.00	0.32±0.06	>19.00	0.32±0.06	Ks
Feulner07	925	20.75 <sup>c</sup>	—	—	—	—	K
This work	1584,194	19.5,20.0 <sup>c</sup>	[15.0,17.0]	0.53±0.02	[18.0,20.0]	0.33±0.03	Ks

<sup>a</sup>3 $\sigma$  limit for point sources

<sup>b</sup>50% efficiency for point objects

<sup>c</sup>the latest magnitude bin in the number counts

<sup>d</sup>80% efficiency for point objects

Table 6. Characteristics of the surveys in the J band

Reference	Surveyed area sqarcmin	limit magnitude	bright range	bright slope	faint range	faint slope	filter
Bershady98	1.5	24.5 <sup>b</sup>	—	—	>19.5	0.35	J
Teplitz99	180	21.75 <sup>c</sup>	—	—	—	—	J
Saracco99	20	23.75 <sup>c</sup>	—	—	[18.0,24.0]	0.36	J
Väisänen00	2520,1275	18.25,19.25 <sup>c</sup>	[17.0,19.5]	0.40-0.45	—	—	J
Martini01	180,27	18.5,20.5 <sup>c</sup>	[16.0,20.5]	0.54	—	—	J
Maihara01	4	26.25 <sup>c</sup>	—	—	[21.1,25.1]	0.23	J
Saracco01	13.6	24.25 <sup>c</sup>	—	—	>20	0.34	J
Iovino05	391	22.25 <sup>c</sup>	[17.25,22.25]	0.39±0.06	—	—	J
Feulner07	925	22.25 <sup>c</sup>	—	—	—	—	J
Imai07	750,306	19.625,20.375 <sup>c</sup>	[17.0,19.5]	0.39±0.02	>19.5	0.30±0.03	J
This work	1588,392	21.0,22.0 <sup>c</sup>	[17.0,18.5]	0.44±0.04	[19.5,22.0]	0.34±0.01	J

<sup>a</sup>3 $\sigma$  limit for point sources

<sup>b</sup>50% efficiency for point objects

<sup>c</sup>the latest magnitude bin in the number counts

Table 7. Characteristics of the surveys in the H band

Reference	Surveyed area sqarcmin	limit magnitude	bright range	bright slope	faint range	faint slope	filter
Teplitz98	35.4	22.8 <sup>a</sup>	—	—	—	—	F160W
Yan98	8.7,2.9	23.5,24.5 <sup>c</sup>	—	—	[20,24.5]	0.315±0.02	F160W
Thompson99	0.7	27.4 <sup>b</sup>	—	—	—	—	F160W
Martini01	180,80	18.0,19.0 <sup>c</sup>	<19	0.47	—	—	H
Chen02	1408	20.8 <sup>d</sup>	<19	0.45±0.01	>19	0.27±0.01	H
Moy03	97.2,619	20.5,19.8 <sup>b</sup>	—	—	—	—	H
Metcalfe06	49	22.9 <sup>a</sup>	—	—	—	—	H
Metcalfe06-Nicmos	0.90	27.2 <sup>c</sup>	—	—	—	—	F160W
Frith06	1080	17.75 <sup>c</sup>	—	—	—	—	H
This work	1598,594	20.5,21.0 <sup>c</sup>	[15.5,18.0]	0.46±0.02	[19.0,21.0]	0.36±0.01	H

<sup>a</sup>3 $\sigma$  limit for point sources

<sup>b</sup>50% efficiency for point objects

<sup>c</sup>the latest magnitude bin in the number counts

<sup>d</sup>S/N=5 in a 4'' diameter aperture

tical data and independent determinations of the local luminosity functions, allow evolution to be examined, in particular the still uncertain question of the formation and evolutionary history of early type galaxies.

In this section we compare our counts with semi-analytic predictions from number-count models, following the recipes given in Gardner (1998), which trace back the redshift evolution of the galaxy Spectral Energy Distribution (SED) of different galaxy classes. The SEDs have been computed using the codes of Bruzual & Charlot (2003). We apply dust attenuation following Eliche-Moral et al. (2006),  $\tau_B = 0.6$  that corresponds to  $\tau_V = 0.4$  if the attenuation follows a  $\propto \lambda^{-2}$  power law. We apply dust extinction either directly and by the same amount to all the galaxies using Bruzual & Charlot (2003) codes, following the prescription given in Charlot & Fall (2000), or by using the luminosity dependent extinction law proposed in Wang (1991). The parameters we use to characterize four different galaxy types are given in Tab. 8. In the LF parameterization for the different bands,  $M^*$  is changed according to the rest-frame colors of the evolved SED (from  $z_f$  to  $z = 0$ ), whereas  $\alpha$  and  $\phi^*$  are assumed to be the same in all filters.

In the first step we compare the ALHAMBRA NIR counts with the prediction obtained using the model proposed in Cristóbal-Hornillos et al. (2003). The extinction correction was applied directly to the SEDs, as an entry parameter in the code described in Bruzual & Charlot (2003) using  $\tau_V = 1.2$  for stars younger than  $10^7$ yr, and  $\mu = 0.3$  as the fraction of it coming from an ambient contribution which affects the old stars too. The parameters used in the local luminosity function are  $M^* = -24.07$ ,  $\alpha = -1.00$ ,  $\phi^* = 4.94 \times 10^{-3}$  calculated in Gardner et al. (1997) (Cole et al. (2001) provide the parameters for the  $\Lambda$ -cosmology), which were transformed to take into account the presence of different galactic types in the local LF adopting the galaxy mixing E/S0=28%, Sab/Sbc=47%, Scd=13%.

The model also adds a dwarf star-forming population, characterized by an stellar population of age 1Gyr at all redshifts, and a steeper slope LF ( $M^* = -23.12$ ,  $\alpha = -1.5$ ,  $\phi^* = 0.96 \times 10^{-3}$ ) given in Gardner (1998). The formation redshifts are  $z_f = 2.0$  for the E/S0 and intermediate-type disk galaxies and  $z_f = 1.0$  for the Scd, although the formation redshift for the Scd could be  $z_f = 4.0$  or higher without modifying the total counts in NIR, that at magnitudes fainter than  $K_s=21.5$  are dominated by the dwarf star-forming population. Due to the disappearance of the red-galaxy population at  $z > 2.0$  this model reproduces the change of slope in the  $K_s$  band observed in the present data (see Fig. 19).

However, as it was discussed in Eliche-Moral et al. (2006), this model fails to simultaneously reproduce the blue band counts as can be seen in Fig. 21, where the predicted counts are compared with some B-band galaxy counts from the literature.



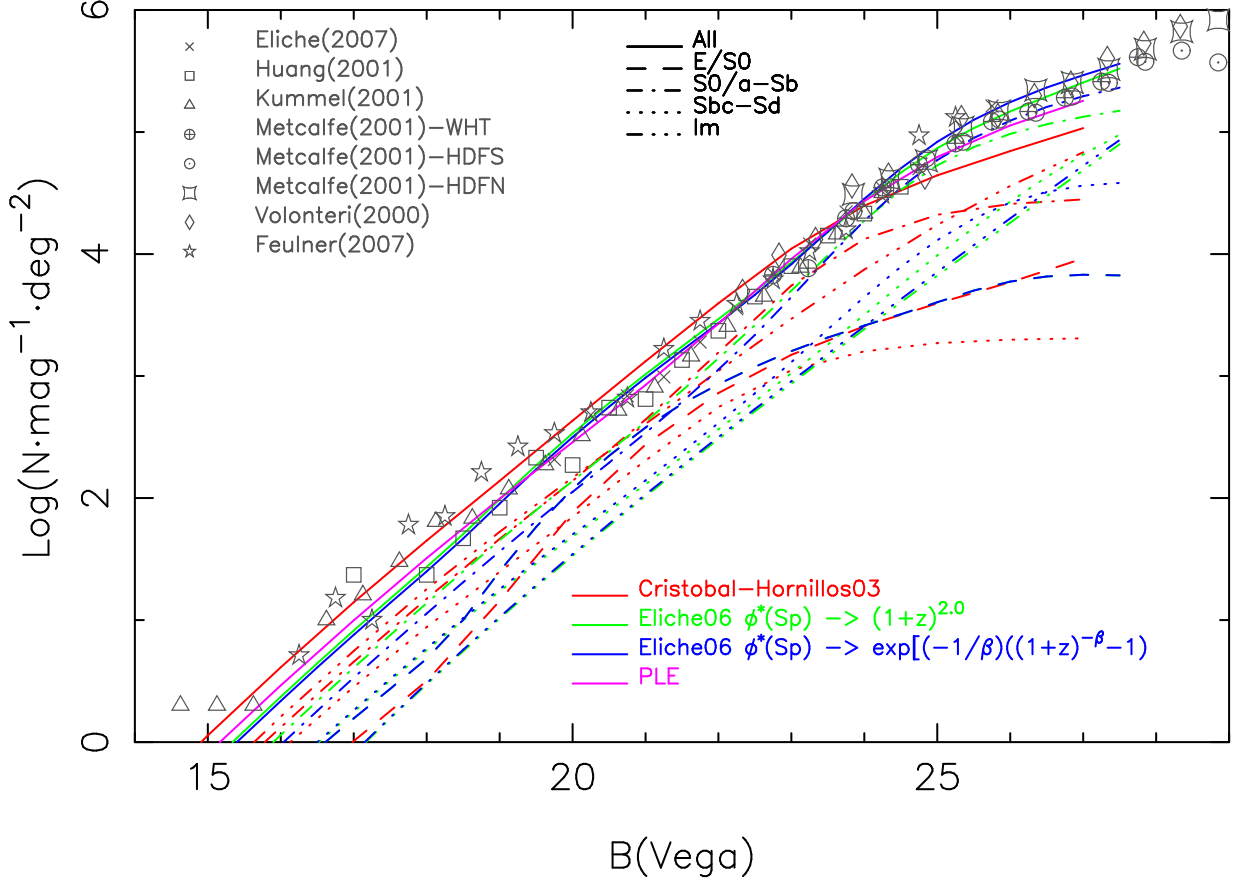


Fig. 21.— Galaxy number count in B band taken from the literature. The lines correspond to the number counts predictions from the models in Cristóbal-Hornillos et al. (2003) and Eliche-Moral et al. (2006). Also it is shown a model where only the passive evolution of stellar populations is considered (PLE).

The number counts models that we consider now, below, include some modifications which aim to simultaneously reproduce the counts in both the NIR filters and blue filters. For these, the local type dependent luminosity functions were computed from Sloan data in Nakamura et al. (2003), as shown in Tab. 9.

We consider first the two models proposed in Eliche-Moral et al. (2006). In the first model a  $\phi^*$  evolution  $\propto (1+z)^2$ , driven via mergers, is considered for the spiral and irregular galaxies. This evolution in  $\phi^*$  is compensated by the evolution in  $M^*$  to conserve the luminosity density. Is it important to take in mind that these models calculate the galaxy number counts tracing back the evolution of the stellar populations to  $z = 0$ , so the intrinsic brightening with  $z$  of the stellar populations must be added to the  $M^*$  evolution when is compared with luminosity functions computed at higher redshifts. The formation redshift for the majority of the ellipticals and intermediate type disk galaxies in this model was set to 1.5. In the second model, the low formation redshift for the early spiral galaxies could be set to  $z_f = 4$ , avoiding at the same time an unreasonable high number of late type galaxies at high- $z$ , using the merger parameterization  $\phi^* \propto \exp[(-Q/\beta)((1+z)^{-\beta} - 1)]$  given in Broadhurst et al. (1992). The value of  $\beta = 1 + (2q_0)^{0.6}/2$  was set to 1.53 using  $q_0 = -0.55$ . A value of  $Q = 1$  was used as in Eliche-Moral et al. (2006). The extinction correction, which is important in the blue bands, was set to  $\tau_B = 0.6$  with the prescription given in Wang (1991). As is shown in Figs. 17 and 18 these two models, that fit the B (Fig. 21) and Ks (Fig. 19) galaxy counts, overestimate the slope variation at J~19 in the Alhambra counts, and at H~18 in data from other surveys.

In order to explain the change of slope in the NIR galaxy counts, the population of red Elliptical galaxies has to decrease with the redshift. Although a model taking into account only the stellar evolution with look back time fits the blue band counts (see Fig. 21), this model over-predicts the faint counts in the NIR bands as can be seen from Fig. 19. Due to the red color of the slope change only the Elliptical population parameterized with a short burst of star-formation can play this role. Fig. 22 shows the evolution with redshift

Table 8. Parameters for the SEDs

Galaxy type	functional form	$\tau$	$Z/Z_\odot$	IMF
E/S0	Single star pop.	—	1	Salpeter
early Sp	Exponential	4	1	Salpeter
late Sp	Exponential	7	2/5	Salpeter
Im	Constant	..	1/5	Salpeter

of the J-H and J-Ks colors for an Elliptical galaxy and an early spiral formed at  $z=4$  (with stellar populations according to the parameters in Tab. 8, and reddening in the spectra applied directly from the Bruzual & Charlot (2003) code using  $\tau_V = 0.8$  and  $\mu = 0.5$ ). The estimated colors of the slope change from the fits given in Tab. 4 are  $J-H \sim 0.97 \pm 0.03$  and  $J-Ks \sim 1.84 \pm 0.03$ , providing evidence that the Elliptical population at  $z \sim 1$  must be the responsible of the turn down of the NIR counts.

In the next model we introduce number-density evolution of the elliptical population parameterized using  $\phi^* \propto (1+z)^{-2}$ . The formation redshifts is set to  $z_f = 4.0$  for all galaxy types, being in more agreement with the evolved red galaxies found at  $z > 2$  (van Dokkum et al. 2003; Daddi et al. 2004). The evolution in the early type densities was not accompanied by an evolution in  $M^*$ , arguing that a substantial number of ellipticals formed in spiral-spiral mergers as expected for hierarchical galaxy formation. For the early spiral galaxies no number-density evolution was considered, and the density evolution parameterization in Eliche-Moral et al. (2006)  $\phi^* \propto (1+z)^2$  was used for the two later type galaxies. The reddening in the spectra was applied directly from the Bruzual & Charlot (2003) code using  $\tau_V = 0.8$  and  $\mu = 0.5$ . This model, as can be seen in the Figs. 23, 24, 25, and 26 fits the galaxy counts in the optical and NIR filters, reproducing the feature of the slope turn down in the three NIR filters.

In order to avoid an unreasonable high number of late type galaxies at high- $z$ , the simple merger evolution  $\phi^* \propto \exp[(-Q/\beta)((1+z)^{-\beta} - 1)]$  given in Broadhurst et al. (1992) could be used with similar results. In this case, we used  $Q=-3$  to parameterize the decrease in number of E/S0 galaxies, and  $Q=1$  to produce the required merger rate in the late spirals and irregulars. The number evolution given by these parameterizations are displayed in Fig 27, showing that at  $z \sim 1$  the implied number density of E/S0 galaxies is only  $\sim 1/4$  of the present day  $\phi^*(0)$ . Density evolution in the early type galaxies was observed in previous works studying the type-dependent LF evolution (Kauffmann et al. 1996; Fried et al. 2001; Aguerri & Trujillo 2002; Wolf et al. 2003; Giallongo et al. 2005; Ilbert et al. 2006). Wolf et al. (2003) found an increase in  $\phi^*$  of an order of magnitude for the early type galaxies from  $z \sim 1.2$  to  $z = 0$ , that is over the  $\phi^* \propto (1+z)^{-2}$  simulated here. However, they used the spectra of a present day Sa type galaxy to separate the different galaxies, which leads to an over-estimation of number-density evolution for the Early-type group.

In Abraham et al. (2007) it is shown that evolution in the fraction of the stellar mass locked in massive early-type galaxies is produced in the interval  $0.7 < z < 1.7$ . A model in which  $\phi^*$  for the Elliptical galaxies is constant to  $z \sim 0.6$  and then evolve as  $\phi^* \propto (0.4+z)^{-2}$  for higher redshifts also produces a good fit to the optical and NIR counts (see Figs. 23, 24, 25, and 26). In this model the population of red elliptical galaxies has doubled since

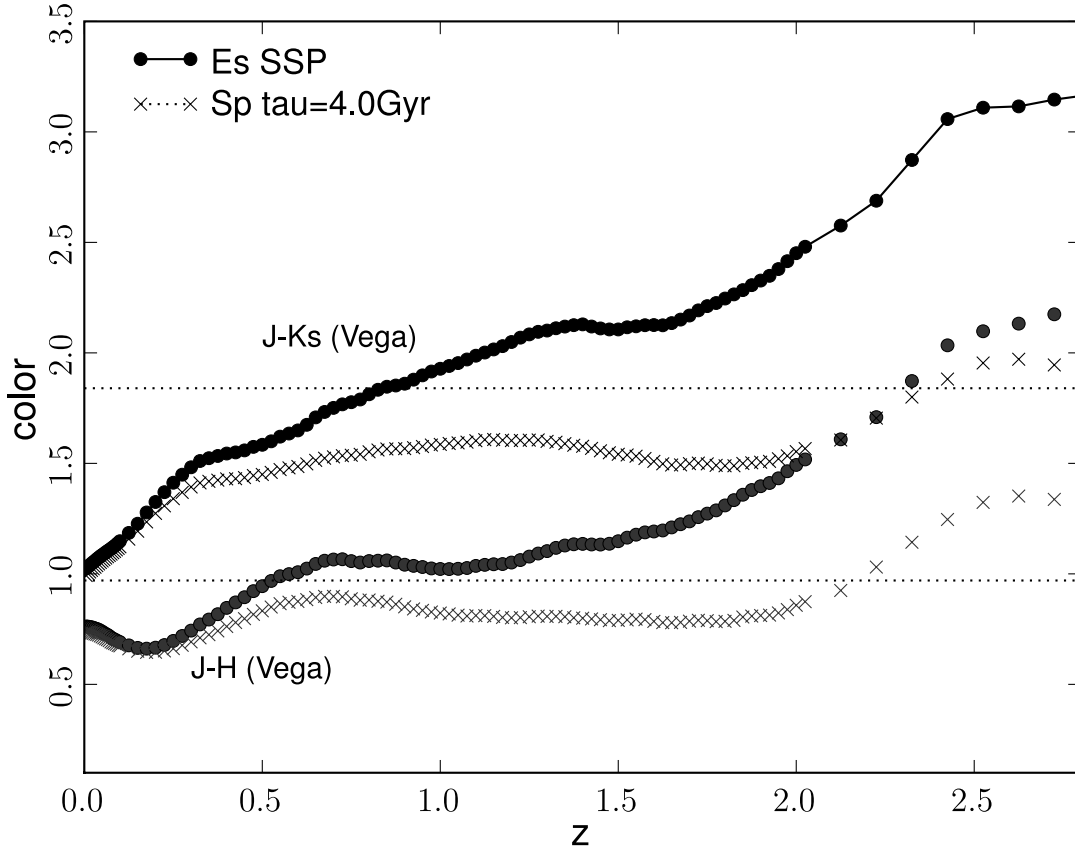


Fig. 22.— Color evolution with redshift of the NIR colors for an Elliptical and an early spiral (with the parameterizations given in Tab. 8). The two upper lines correspond to the J-Ks color whereas the other two correspond to the J-H color. The horizontal dotted lines correspond to the  $J-H \sim 0.97$  and  $J-Ks \sim 1.84$  colors of the fitted point for the slope change.

Table 9. Schechter Parameters for the Luminosity Functions <sup>a</sup>

Galaxy type	$M_{AB}^*(r')$ <sup>b</sup>	$\phi^* \times 10^{-3} Mpc^{-3}$	$\alpha$
E/S0	-21.53	1.61	-0.83
early Sp	-21.08	3.26	-1.15
late Sp	-21.08	1.48	-0.71
Im	-20.78	0.37	-1.90

<sup>a</sup>Considering  $H_0 = 70$

<sup>b</sup>The characteristic galaxy luminosity given in the Sloan  $r'$  band in AB system.

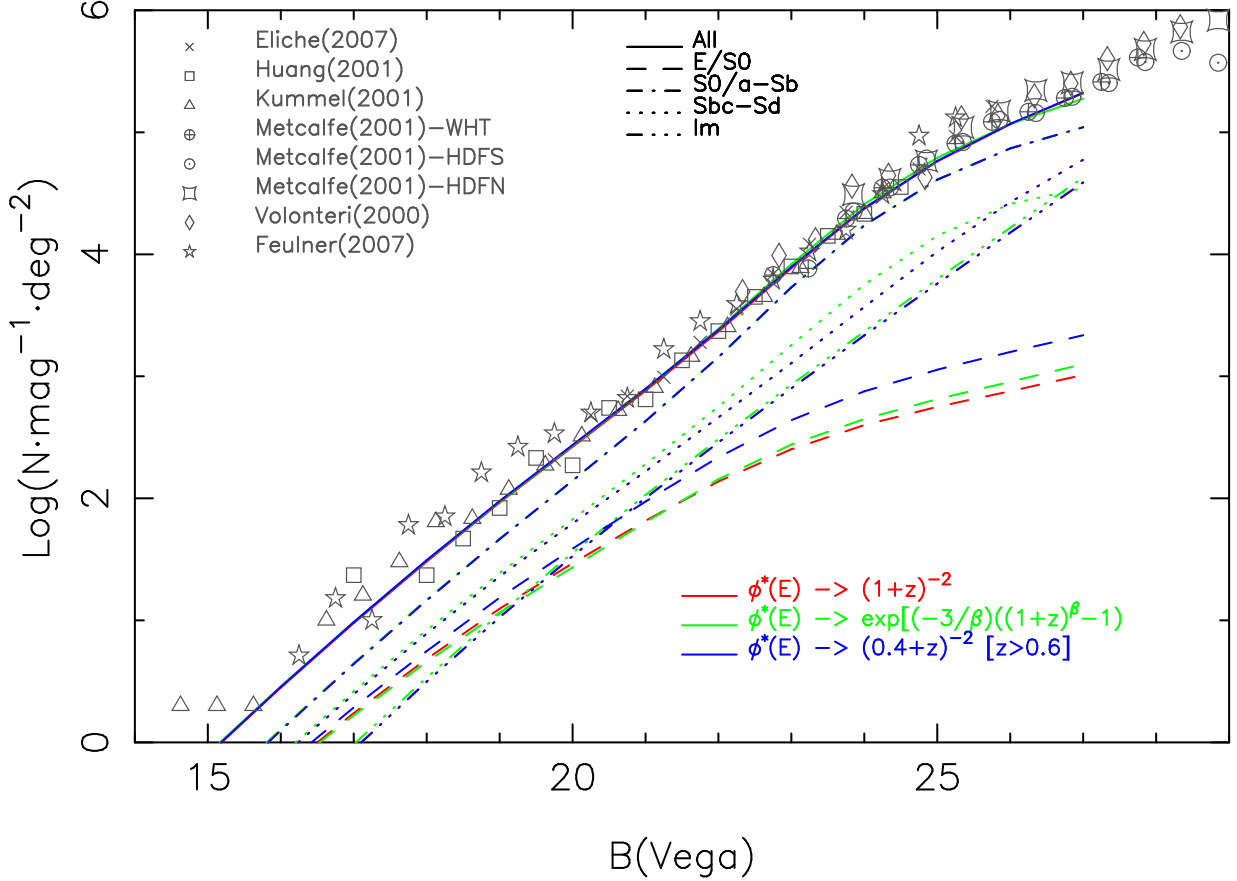


Fig. 23.— Galaxy number count in B band taken from the literature. The lines correspond to the number counts predictions from the models described in the text.

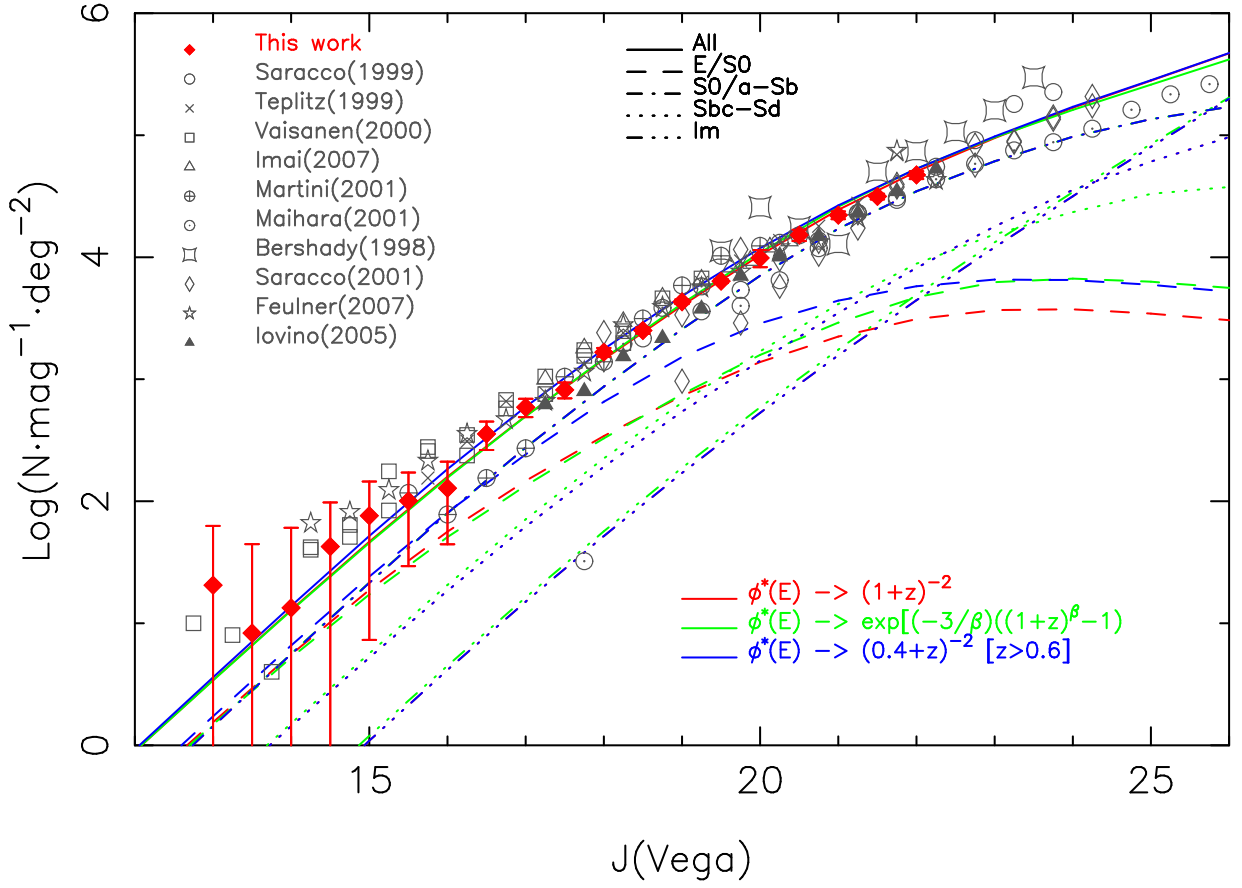


Fig. 24.— Galaxy number counts in the J filter compared with data from other surveys. The lines correspond to number counts models described in the text.

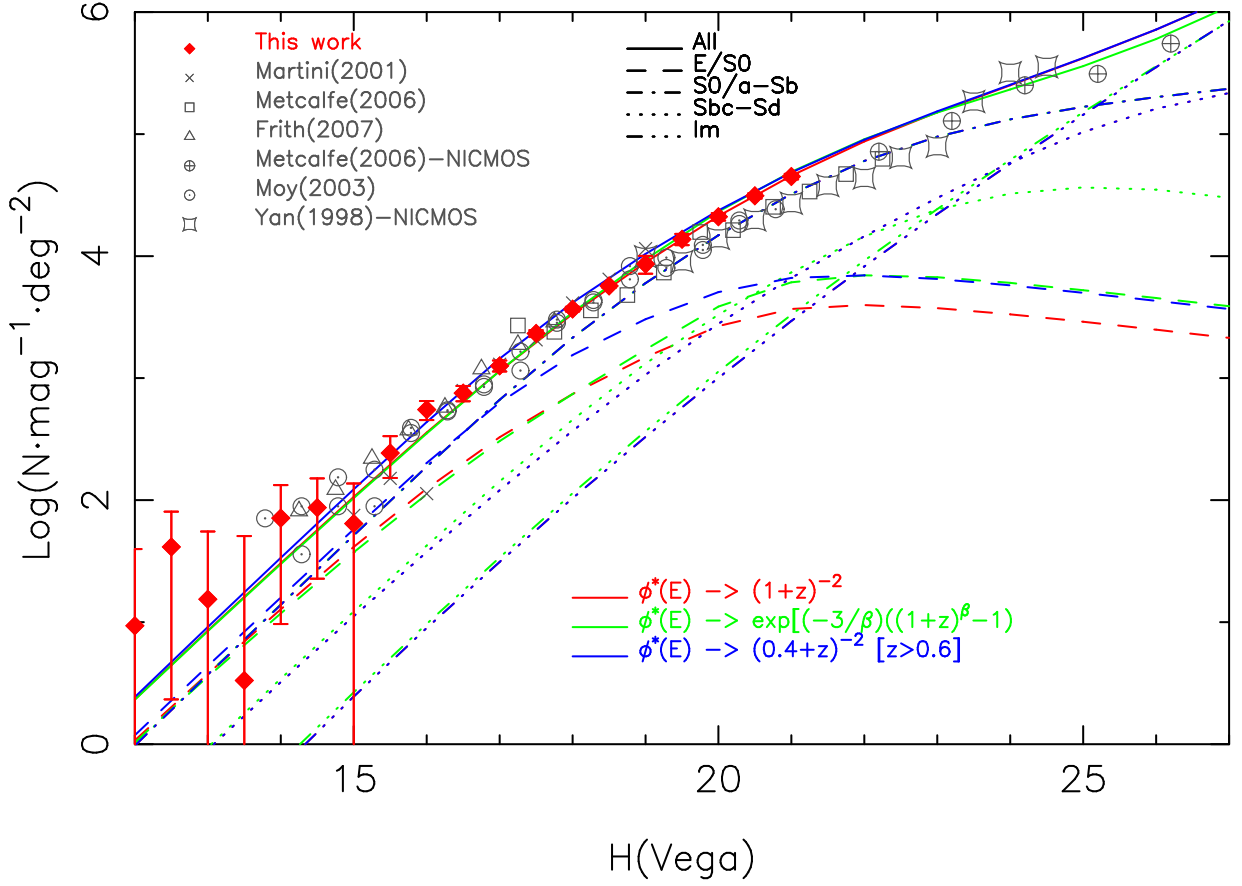


Fig. 25.— Galaxy number counts in the H filter compared with data from other surveys and the number count models described in the text.

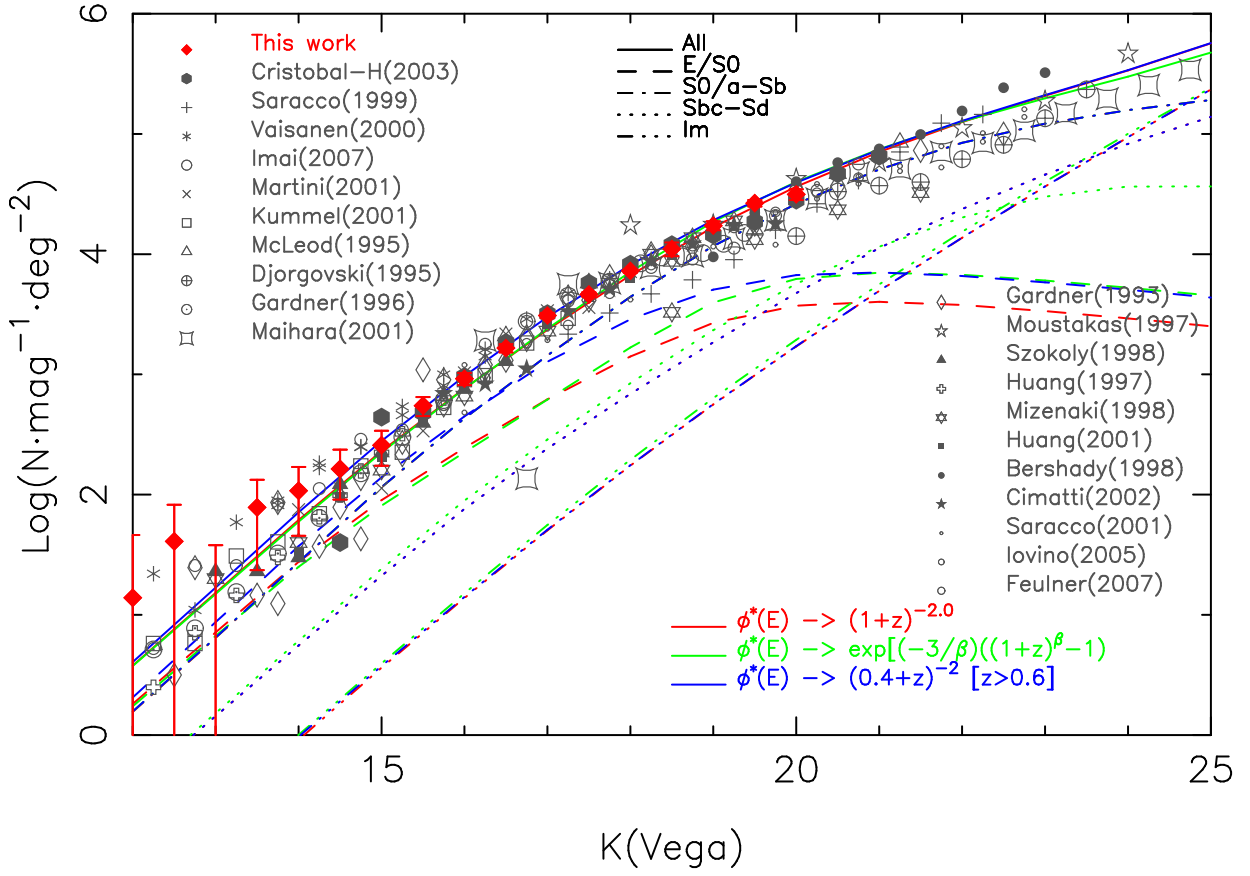


Fig. 26.— Galaxy number counts in the Ks filter compared with data from the literature and the galaxy counts models described in the text.



$z = 1$ , in good agreement with the increase of a factor of  $\sim 2$  in the number evolution of red galaxies given in Bell et al. (2004).

Finally, we have implemented a simple recipe to simulate downsizing in the elliptical population by maintaining  $\phi^*$  constant with redshift for the LF of bright galaxies. The results are compatible with our NIR galaxy counts and B-band counts from the literature in the case that  $\phi^*$  is constant with redshift for red-ellipticals brighter than  $M^* - 0.7$  ( $\sim -22.0$  in the Sloan  $r'$  band in AB system), decreasing the number densities for the bulk of the ellipticals as  $\phi^* \propto (1 + z)^{-2}$ .

## 6. Color analysis

More information about the evolution of the galaxy populations could be obtained from color histograms. The separate number counts in each band at the magnitude ranges that we are sampling are less sensitive to the formation redshift (for values  $zf \geq 4$ ) or the e-folding timescale of the star formation than color histograms. Figure 28 shows the color-magnitude diagram builded with the ALHAMBRA data through the filter centered at 6130 Å (F613) and Ks. The modelled evolutionary tracks for the 4 galaxy spectra considered in Tab. 8 are also displayed. Models with no evolution (top panel) and passive evolution (bottom panel) have been considered. As can be appreciated the evolved spectra produce better match to the data than the no evolved version, principally at the faint blue end which is better described by models considering passive evolution in the late Sp and Irr spectra.

In Fig. 29 it is shown the F613-Ks color histogram for different Ks magnitude bins. We have used an e-folding timescale  $\tau = 0.7$  Gyr to describe the Elliptical galaxies in those plots, this longer timescale produce better fits to the red end of the color histograms than an instantaneous star forming event which over-predict the number of red galaxies. Both models produce similar results when fitting the galaxy counts in individual optical and NIR bands. The simulated histograms correspond to models where the population of E/S0 galaxies decrease with redshift, the population of spirals stay constant, and the late type galaxies increase as  $\phi^* \propto (1 + z)^2$  conserving the luminosity densities. The population of early spiral galaxies have been divided in two classes: one remain as in Tab. 8, whereas the amount of extinction have been doubled for the other. This try to avoid the fact that the discretization of the actual galaxy population in four classes tend to produce sharp histograms.

As can be appreciated the models reproduce the overall shape of the data for bright Ks magnitudes. Nevertheless, at faint Ks magnitudes the models predict higher values in

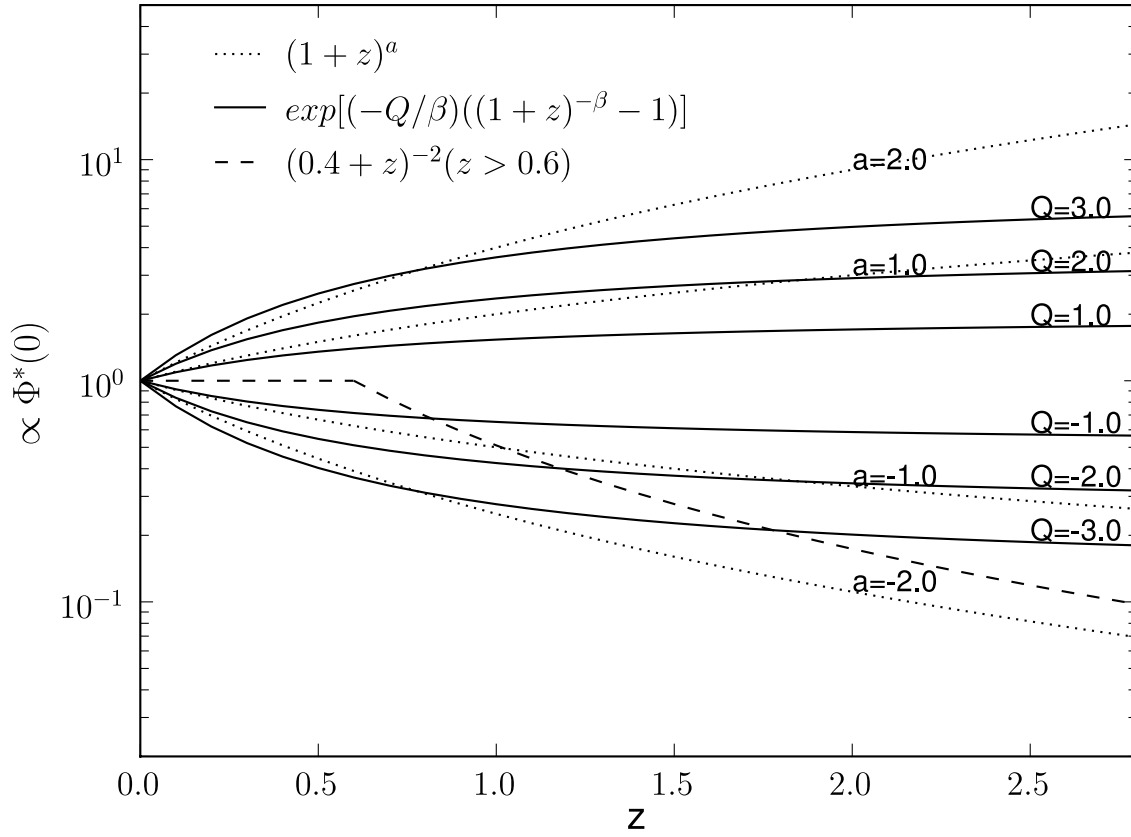


Fig. 27.— Functional form of the  $\phi^*$  evolution parameterization.

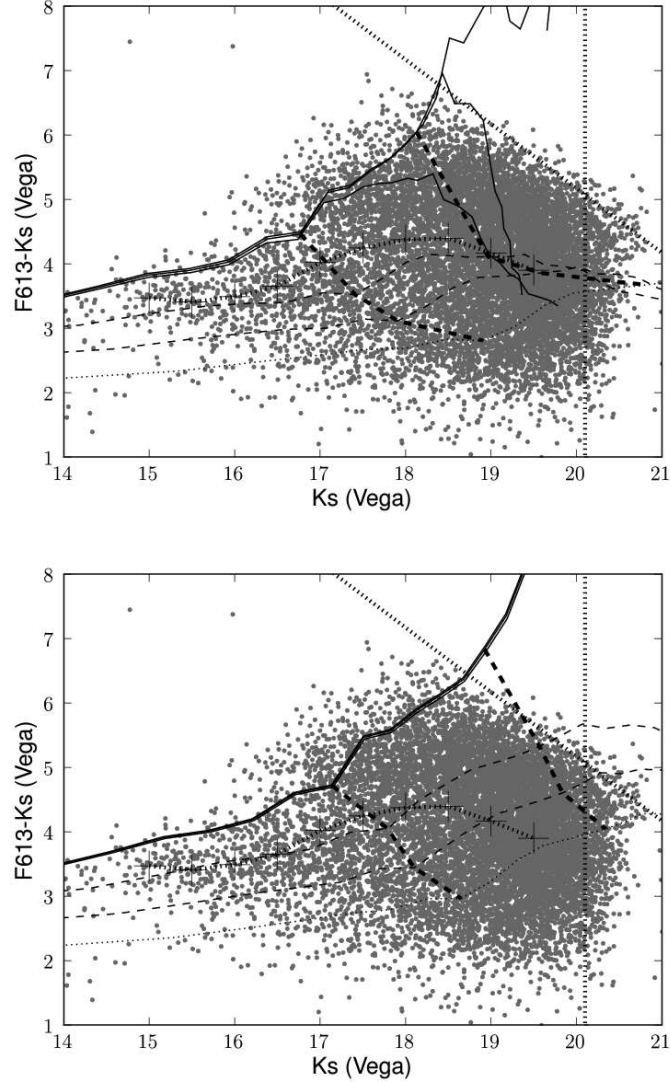


Fig. 28.— Color-magnitude diagram for the Alhambra data in the filter with effective wavelength  $6130\text{\AA}$  (F613) and Ks. The tracks for the galaxy classes in Tab. 8 formed at  $z_f=4$  are also shown, for the passive evolution scenario *top panel*), and the no-evolution case *bottom panel*). Each galaxy track is computed for the characteristic luminosity given in Tab. 9. The solid tracks from top to bottom correspond to a simulated E/S0 galaxy with single stellar population and e-folding timescales  $\tau = 0.5, 1\text{Gyr}$ . The dashed lines correspond to the early and late type spiral galaxies, and the dotted line to the Irr galaxy. The vertical dotted line and the diagonal one are the  $5\sigma$  detection levels. The two dashed lines join the spectra points for  $z=0.5$  and  $z=1.0$ . The median color for each Ks bin is marked with crosses.

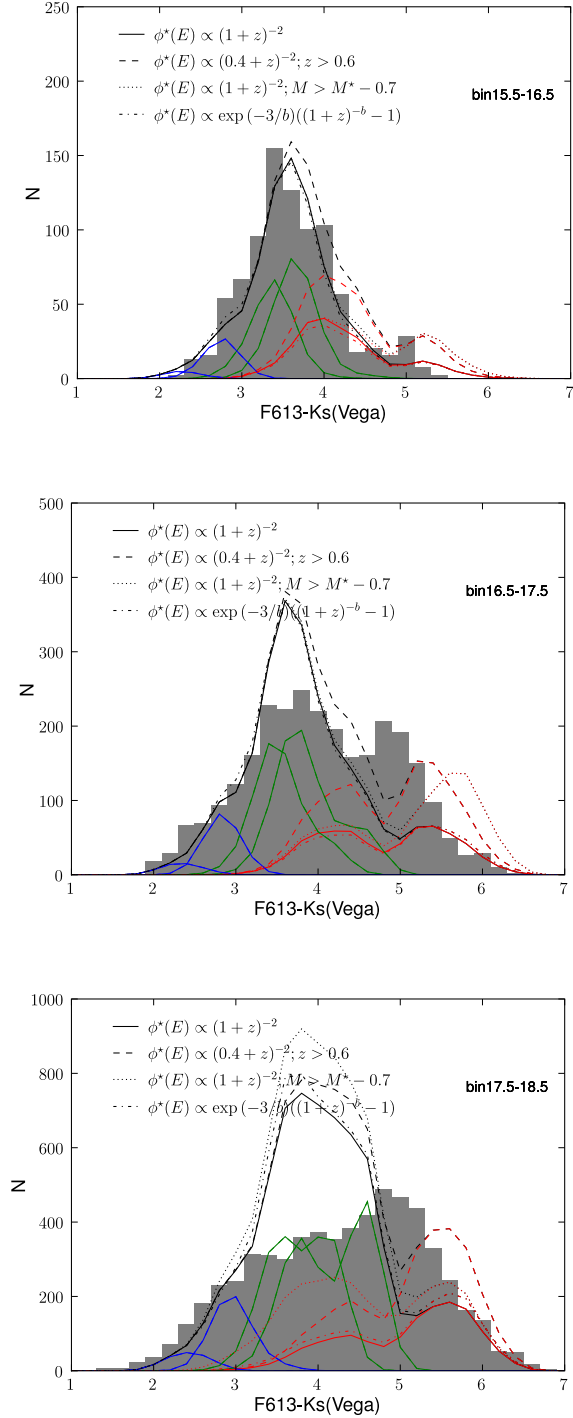


Fig. 29.— Color F613-Ks histogram (normalized for 1 square degree) for sources in different Ks bins. The histograms produced by the models have been convolved with a Gaussian kernel  $\sigma = 0.2$  in order to reproduce the photometric errors. The histograms computed for each population are shown in red for the E/S0, green for the early type spiral galaxies, and in blue for the late type spirals and Irr galaxies.

the color range  $3 \leq F613 - Ks \leq 5$ . As could be inferred from Fig. 29 to obtain a better match to the data the number densities of early spiral galaxies formed in a shorter time-scale has to decrease with  $z$ , such fading of the spirals will lead to an under-prediction of the blue-band number counts unless that the number of star-forming increases at higher redshift. In Fig. 30 the F613-Ks histograms for the Ks bins: [16.5,17.5], [17.5,18.5] show a better concordance with the observed data. Those histograms correspond to a models where the number densities for the early spirals decrease with  $z$  as  $\phi^* \propto (1+z)^{-1}$ , the late type spirals number density remain constant with redshift, and number densities of Irr galaxies increase  $\propto (1+z)^3$ . The luminosity density is not conserved within any galaxy class. Similar results could be obtained using  $\phi^* \propto \exp [(-Q/\beta)((1+z)^{-\beta} - 1)]$  (Broadhurst et al. 1992), with  $Q=-1$ , and  $Q=3$  to describe the number evolution of early spiral and Irr galaxies. This number evolution formulation avoid a step increase of Irr galaxies at high redshift. However in Fig. 30 a shortage of red galaxies is seen at about  $F613-Ks \sim 5$ , this could be due to the fact that we only use a discrete number of galaxy parameterizations, for example is well know the existence of dusty starburst with the same red colors than the passive extremely red objects (Daddi et al. 2000). Covering a wider range in galaxy internal extinction or formation timescale will tend to smear the bi-modality present in the simulated histograms. As could be seen in Fig. 31 the number counts produced by this model in B + NIR filters also produce good fits to the observed data points. In this models the number counts at faint magnitudes will be dominated by the star-forming galaxies. The number count slope at faint magnitudes will be  $-0.4(\alpha + 1)$  (Bershady 2003), being  $\alpha$  the slope of the dominant luminosity function for  $M \ll M^*$ . With this parameterization the slope of the number counts tend to 0.36 at the fainter end.

## 7. Summary

We have presented galaxy counts in the J,H, and Ks filters covering an area of 0.45 square degrees and an average 50% detection efficiency depth of  $J \sim 22.4$ ,  $H \sim 21.3$  and  $Ks \sim 20.0$  (Vega system). The depth reached, and the precision of the counts over a range of five magnitudes makes the data valuable for examining the change of the count slope reported in the Ks filter, and to extend this examination to the J and H bands. We find that a change in slope occur in each of the NIR bands in the range  $J=[18.5,19.5]$ ,  $H=[18.0,19.0]$  and  $Ks=[17.0,18.0]$ . The NIR colors where the break in the galaxy counts are found imply that this change is related to the population of red galaxies at  $z \sim 1$ .

We have compared our number counts results with predictions from a wide range of number count models, concluding that in order to reproduce the described changes in the NIR slopes, a decrease in bulk of the population of red elliptical galaxies is needed. Good fits to the B-band and NIR counts are obtained with a parameterization for the number evolution of the elliptical population as  $\phi^* \propto (1+z)^{-2}$  with no accompanying evolution in  $M^*$ , corresponding to evolution in which the majority of ellipticals formed in spiral-spiral mergers.

Performing a color analysis show that also the population of early spirals has to decrease at higher redshift in order to describe the color distribution in r-Ks. Models using the parameterization of Broadhurst et al. (1992)  $\phi^* \propto \exp [(-Q/\beta)((1+z)^{-\beta} - 1)]$ , with  $Q=-3$ ,  $Q=-1$ , and  $Q=3$  to describe the number evolution of ellipticals, early spiral and Irr galaxies, with no number density evolution for late-spiral systems, produce good fits to the observed distribution, avoiding at the same time a high number of young systems at high  $z$ . A good match to the optical and NIR data is also obtained if the population of red-galaxies in the models remain constant to  $z \sim 0.6$  and afterwards its number density decrease as  $\phi^* \propto (0.4+z)^{-2}$ , or if the number density of red-ellipticals is constant with redshift for galaxies brighter than  $M^* - 0.7$  ( $\sim -22.0$  in the Sloan  $r'$  band in AB system), decreasing as  $\phi^* \propto (1+z)^{-2}$  for the bulk of the ellipticals.

Alhambra is processing the data obtained in 20 medium-band optical and 3 NIR filters reaching high quality photometric redshift measurements ( $\Delta z/(1+z) \leq 0.03$ ). Also an accurate classification by Spectral Energy distribution will be acquired. Those data will allow for the study of the evolution of the different galaxy types to  $z \sim 1$ , which will complement the results given in this article, disentangling what populations contribute to the number counts at different redshift intervals. Also the study of number counts for red galaxy populations, passive EROS or BzK (Daddi et al. 2004) galaxies will constrain the formation redshift and formation timescale for massive Elliptical galaxies.

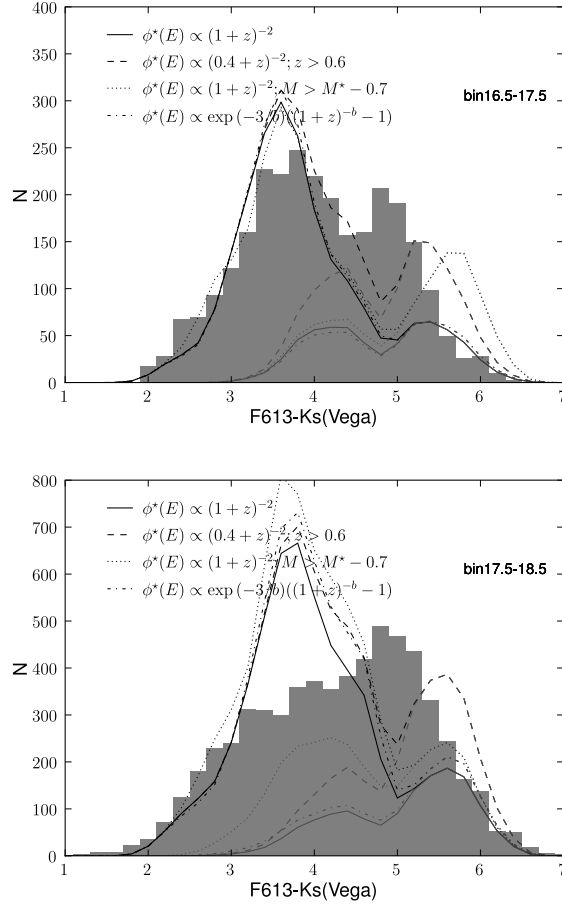


Fig. 30.— Color F613-Ks histogram for sources in different Ks bins. The histograms have been normalized to 1 square degree. The modelled histograms have been computed for models in which the number densities for the early spirals decrease with redshift as  $\phi^* \propto (1+z)^{-1}$ , the late type spirals number density remain constant with redshift, and number densities of Irr galaxies increase  $\propto (1+z)^3$ . The number of E/S0 galaxies decrease with  $z$  as specified in the labels. The histograms obtained with this models have been convolved with a Gaussian kernel  $\sigma = 0.2$  in order to reproduce the photometric errors.

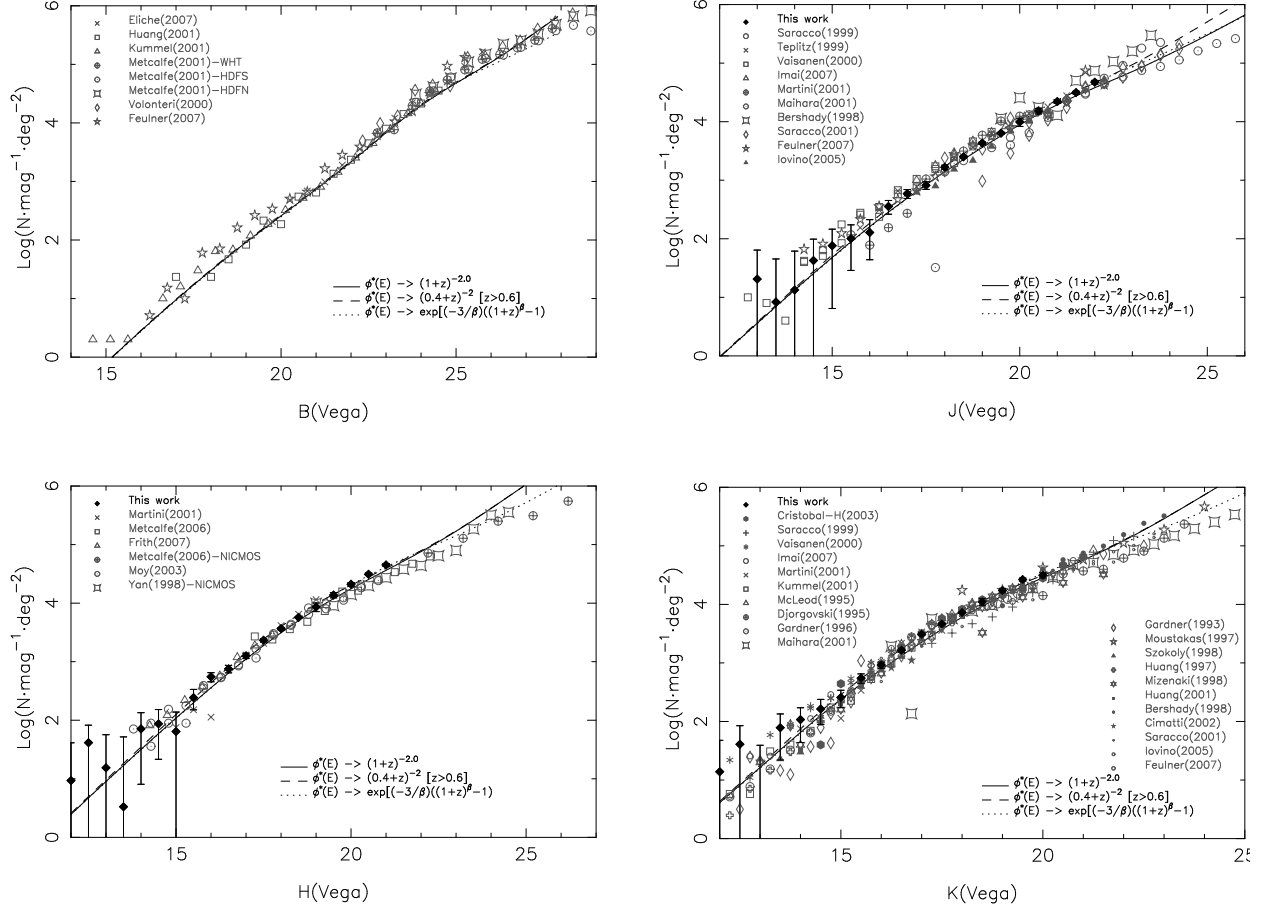


Fig. 31.— Differential number counts in the B and NIR bands compared with a models in which the number densities for the early spirals decrease with redshift as  $\phi^* \propto (1+z)^{-1}$ , the late type spirals number density remain constant with redshift, and number densities of Irr galaxies increase  $\propto (1+z)^3$ .



The authors acknowledge support from the Spanish Ministerio de Educación y Ciencia through grants AYA2002-12685-E, AYA2003-08729-C02-01, AYA2003-0128, AYA2007-67965-C03-01, AYA2004-20014-E, AYA2004-02703, AYA2004-05395, AYA2005-06816, AYA2005-07789, AYA2006-14056, and from the *Junta de Andalucía*, TIC114, TIC101 and *Proyecto de Excelencia* FQM-1392. NB, JALA, MC, and AFS acknowledge support from the MEC *Ramón y Cajal* Programme. NB acknowledges support from the EU IRG-017288.

This work has made use of software designed at TERAPIX.

This publication makes use of data products from the Two Micron All Sky Survey, which is a joint project of the University of Massachusetts and the Infrared Processing and Analysis Center/California Institute of Technology, funded by the National Aeronautics and Space Administration and the National Science Foundation

This publication makes use of data from the Sloan Digital Sky Survey. Funding for the Sloan Digital Sky Survey (SDSS) has been provided by the Alfred P. Sloan Foundation, the Participating Institutions, the National Aeronautics and Space Administration, the National Science Foundation, the U.S. Department of Energy, the Japanese Monbukagakusho, and the Max Planck Society. The SDSS Web site is <http://www.sdss.org/>.

The SDSS is managed by the Astrophysical Research Consortium (ARC) for the Participating Institutions. The Participating Institutions are The University of Chicago, Fermilab, the Institute for Advanced Study, the Japan Participation Group, The Johns Hopkins University, Los Alamos National Laboratory, the Max-Planck-Institute for Astronomy (MPIA), the Max-Planck-Institute for Astrophysics (MPA), New Mexico State University, University of Pittsburgh, Princeton University, the United States Naval Observatory, and the University of Washington.

### **A. Individual image combination**

As mentioned in the text, to combine the processed images we used SWARP (Bertin et al. 2002). With this software, individual images were projected into subsections of the final frame using the inverse mapping, in which each output pixel center was associated to a position in the input image at which it is interpolated. With this schema, the code corrected at the same time the geometrical distortions in the individual images using the astrometric information stored in the image headers.

### A.1. Estimating the relative transparency

Using a filtered version of the SExtractor catalogs computed over the sky subtracted images, an accurate estimate of the relative transparency was computed by tracing the high S/N objects in all the images. The relative transparency values were used inside SWARP to scale the individual images to the same flux level in order to uniformize the zero points in the outer dither areas, this allowed to use 2MASS catalogs to calibrate the ALHAMBRA NIR photometry in the final images.

### A.2. Astrometry calibration

When computing the resampled version of the individual frames, SWARP uses the WCS information stored in the headers. In order to obtain a better matching of the individual images, firstly the pipeline calculated the external astrometrical solution for a reference image. The individual images were then calibrated internally with respect to it, thus obtaining the equatorial coordinates from the reference image. In this paper the individual image with better transparency in a given pointing was used as reference. However, to get a better internal astrometry between the different filters, after completing a pointing in the 23 ALHAMBRA filters, the images with better FWHM and transparency in a set of selected optical filters, are combined to produce a deep image that will be used afterwards as reference.

We have determined that the USNO-B1.0 catalog (Monet et al. 2003) provides an adequate number of objects to perform a high quality external astrometric calibration. We used our own code to match the sources with brighter apparent magnitudes in the reference image with those in the USNO-B1.0. Once a meaningful number of pairs was identified, the CCMAP IRAF task was used in two iterations to acquire the required astrometric solution with a 2nd order polynomial. A histogram of the external astrometric solution rms and the number of objects used for the final images of ALH08 is shown in Fig. 32. The median external astrometry rms is  $0.12'' \pm 0.01$  in RA and  $0.11'' \pm 0.01$  DEC.

Having calibrated a reference image, the rest of the individual images were calibrated internally. The median internal rms in the astrometric solution for the OMEGA2000 data used in this paper is  $0.06''$  in RA and DEC using a median of 160 objects, as shown in Fig 32.

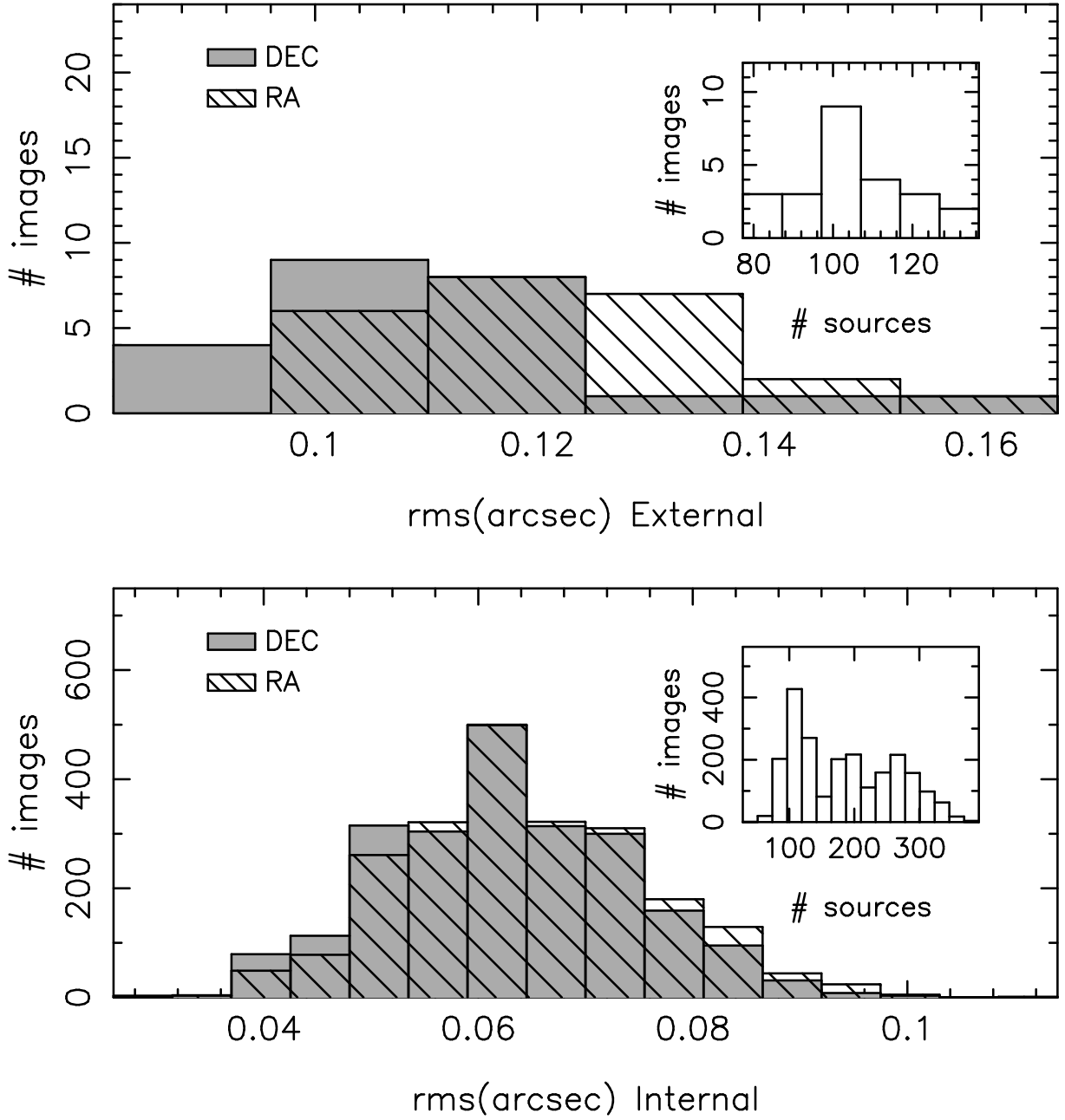


Fig. 32.— Histograms of the astrometry solution rms for the ALH08 images. (*Top panel*) External USNO-B1.0. (*Bottom panel*) internal. The small panels show the histograms of the number of objects that enter into the final astrometry fitting

### A.3. Image co-adding

Swarp allows the user to choose among several interpolation functions for inverse mapping. For selecting the more appropriate kernel we analyzed the resulting final image FWHM and its pixel-to-pixel correlation. Tab. 10 shows the correlation values, between adjacent pixels and for pixel pairs separated by 2 pixels, in the final images obtained using different available interpolation functions. As can be seen in the table, the bilinear function produce a higher correlation which translate into an underestimation of the flux errors. Using the Lanczos-3 function the FWHM of the final image was improved by  $\sim 0.05''$  compared with the nearest neighbor interpolation, whereas the auto-correlation at 1 pixel remain acceptable  $\sim 0.16$  (when the images are combined using the average). The Lanczos-4 function did not decrease substantially nor the FWHM neither the correlation at 1 pixel, on the contrary it produced large artifacts at the bad pixels and image borders, so finally we have decided to take the Lanczos-3 function.

Table 10. Values for the correlation between adjacent pixels when co-adding the images using different interpolation functions

	Nearest	Bilinear	Lanczos2	Lanczos3	Lanczos4
Combining with median					
1pix	+0.017	+0.186	+0.112	+0.074	+0.068
2pix	-0.035	-0.013	-0.072	-0.059	-0.101
Combining with average					
1pix	+0.035	+0.274	+0.177	+0.156	+0.130
2pix	-0.030	-0.018	-0.069	-0.110	-0.083

## REFERENCES

- Abraham, R. G., et al. 2007, *ApJ*, 669, 184
- Aguerri, J. A. L., & Trujillo, I. 2002, *MNRAS*, 333, 633
- Bell, E. F., et al. 2004, *ApJ*, 608, 752
- Benitez et al. 2008, submitted
- Bertin, E., & Arnouts, S. 1996, *A&AS*, 117, 393
- Bertin, E., Mellier, Y., Radovich, M., Missonnier, G., Didelon, P., & Morin, B. 2002, *Astronomical Data Analysis Software and Systems XI*, 281, 228
- Bershady, M. A., Lowenthal, J. D., & Koo, D. C. 1998, *ApJ*, 505, 50
- Bershady, M. A. 2003, *Revista Mexicana de Astronomia y Astrofisica Conference Series*, 16, 203
- Blanton, M. R., et al. 2003, *ApJ*, 592, 819
- Broadhurst, T. J., Ellis, R. S., & Glazebrook, K. 1992, *Nature*, 355, 55
- Bruzual, G., & Charlot, S. 2003, *MNRAS*, 344, 1000
- Capak, P., et al. 2004, *AJ*, 127, 180
- Charlot, S., & Fall, S. M. 2000, *ApJ*, 539, 718
- Chen, H.-W., et al. 2002, *ApJ*, 570, 54
- Cimatti, A., et al. 2002, *A&A*, 392, 395
- Cristóbal-Hornillos, D., Balcells, M., Prieto, M., Guzmán, R., Gallego, J., Cardiel, N., Serrano, Á., & Pelló, R. 2003, *ApJ*, 595, 71
- Cole, S., et al. 2001, *MNRAS*, 326, 255
- Covey, K. R., et al. 2007, *AJ*, 134, 2398
- Cutri, R. M., et al. 2003, The IRSA 2MASS All-Sky Point Source Catalog, NASA/IPAC Infrared Science Archive. <http://irsa.ipac.caltech.edu/applications/Gator/>,
- Daddi, E., Cimatti, A., Pozzetti, L., Hoekstra, H., Röttgering, H. J. A., Renzini, A., Zamorani, G., & Mannucci, F. 2000, *A&A*, 361, 535

- Daddi, E., Cimatti, A., Renzini, A., Fontana, A., Mignoli, M., Pozzetti, L., Tozzi, P., & Zamorani, G. 2004, *ApJ*, 617, 746
- Djorgovski, S., et al. 1995, *ApJ*, 438, L13
- Eddington, A. S. 1913, *MNRAS*, 74, 5
- Eliche-Moral, M. C., Balcells, M., Prieto, M., García-Dabó, C. E., Erwin, P., & Cristóbal-Hornillos, D. 2006, *ApJ*, 639, 644
- Elston, R. J., et al. 2006, *ApJ*, 639, 816
- Faber, S. M., et al. 2007, *ApJ*, 665, 265
- Feulner, G., Goranova, Y., Hopp, U., Gabasch, A., Bender, R., Botzler, C. S., & Drory, N. 2007, *MNRAS*, 378, 429
- Finlator, K., et al. 2000, *AJ*, 120, 2615
- Fontana, A., et al. 2004, *A&A*, 424, 23
- Fried, J. W., et al. 2001, *A&A*, 367, 788
- Frith, W. J., Metcalfe, N., & Shanks, T. 2006, *MNRAS*, 371, 1601
- Gardner, J. P., Cowie, L. L., & Wainscoat, R. J. 1993, *ApJ*, 415, L9
- Gardner, J. P., Sharples, R. M., Carrasco, B. E., & Frenk, C. S. 1996, *MNRAS*, 282, L1
- Gardner, J. P., Sharples, R. M., Frenk, C. S., & Carrasco, B. E. 1997, *ApJ*, 480, L99
- Gardner, J. P. 1998, *PASP*, 110, 291
- Giallongo, E., Salimbeni, S., Menci, N., Zamorani, G., Fontana, A., Dickinson, M., Cristiani, S., & Pozzetti, L. 2005, *ApJ*, 622, 116
- Glazebrook, K., Peacock, J. A., Collins, C. A., & Miller, L. 1994, *MNRAS*, 266, 65
- Huang, J.-S., Cowie, L. L., Gardner, J. P., Hu, E. M., Songaila, A., & Wainscoat, R. J. 1997, *ApJ*, 476, 12
- Huang, J.-S., et al. 2001, *A&A*, 368, 787
- Ilbert, O., et al. 2006, *A&A*, 453, 809
- Im, M., et al. 2002, *ApJ*, 571, 136

- Imai, K., Matsuhara, H., Oyabu, S., Wada, T., Takagi, T., Fujishiro, N., Hanami, H., & Pearson, C. P. 2007, *AJ*, 133, 2418
- Iovino, A., et al. 2005, *A&A*, 442, 423
- Kauffmann, G., Charlot, S., & White, S. D. M. 1996, *MNRAS*, 283, L117
- Kümmel, M. W., & Wagner, S. J. 2000, *A&A*, 353, 867
- Kümmel, M. W., & Wagner, S. J. 2001, *A&A*, 370, 384
- McCracken, H. J., Metcalfe, N., Shanks, T., Campos, A., Gardner, J. P., & Fong, R. 2000, *MNRAS*, 311, 707
- McLeod, B. A., Bernstein, G. M., Rieke, M. J., Tollestrup, E. V., & Fazio, G. G. 1995, *ApJS*, 96, 117
- Maihara, T., et al. 2001, *PASJ*, 53, 25
- Martini, P. 2001, *AJ*, 121, 598
- Metcalfe, N., Shanks, T., Campos, A., Fong, R., & Gardner, J. P. 1996, *Nature*, 383, 236
- Metcalfe, N., Shanks, T., Campos, A., McCracken, H. J., & Fong, R. 2001, *MNRAS*, 323, 795
- Metcalfe, N., Shanks, T., Weilbacher, P. M., McCracken, H. J., Fong, R., & Thompson, D. 2006, *MNRAS*, 370, 1257
- Minezaki, T., Kobayashi, Y., Yoshii, Y., & Peterson, B. A. 1998, *ApJ*, 494, 111
- Moles et al. 2008, *AJ*, in press
- Monet, D. G., et al. 2003, *AJ*, 125, 984
- Moustakas, L. A., Davis, M., Graham, J. R., Silk, J., Peterson, B. A., & Yoshii, Y. 1997, *ApJ*, 475, 445
- Moy, E., Barmby, P., Rigopoulou, D., Huang, J.-S., Willner, S. P., & Fazio, G. G. 2003, *A&A*, 403, 493
- Nakamura, O., Fukugita, M., Yasuda, N., Loveday, J., Brinkmann, J., Schneider, D. P., Shimasaku, K., & SubbaRao, M. 2003, *AJ*, 125, 1682
- Perlmutter, S., et al. 1999, *ApJ*, 517, 565



- Riess, A. G., et al. 1998, *AJ*, 116, 1009
- Robin, A. C., Haywood, M., Creze, M., Ojha, D. K., & Bienayme, O. 1996, *A&A*, 305, 125
- Saracco, P., D’Odorico, S., Moorwood, A., Buzzoni, A., Cuby, J.-G., & Lidman, C. 1999, *A&A*, 349, 751
- Saracco, P., Giallongo, E., Cristiani, S., D’Odorico, S., Fontana, A., Iovino, A., Poli, F., & Vanzella, E. 2001, *A&A*, 375, 1
- Spergel, D. N., et al. 2003, *ApJS*, 148, 175
- Stanford, S. A., Eisenhardt, P. R. M., & Dickinson, M. 1995, *ApJ*, 450, 512
- Szokoly, G. P., Subbarao, M. U., Connolly, A. J., & Mobasher, B. 1998, *ApJ*, 492, 452
- Teerikorpi, P. 2004, *A&A*, 424, 73
- Teplitz, H. I., McLean, I. S., & Malkan, M. A. 1999, *ApJ*, 520, 469
- Väisänen, P., Tollestrup, E. V., Willner, S. P., & Cohen, M. 2000, *ApJ*, 540, 593
- Valdes, F. G. 2002, *Automated Data Analysis in Astronomy*, 309
- van Dokkum, P. G., et al. 2003, *ApJ*, 587, L83
- Volonteri, M., Saracco, P., Chincarini, G., & Bolzonella, M. 2000, *A&A*, 362, 487
- Wang, B. 1991, *ApJ*, 383, L37
- Wolf, C., Meisenheimer, K., Rix, H.-W., Borch, A., Dye, S., & Kleinheinrich, M. 2003, *A&A*, 401, 73
- Yan, L., McCarthy, P. J., Storrie-Lombardi, L. J., & Weymann, R. J. 1998, *ApJ*, 503, L19